Methodical
and Applied Research

UNIVERSAL PROTON AND NEUTRON CENTRE FOR RADIATION RESISTANCE
OF AVIONIC SPACE ELECTRONICS AND OTHER APPLICATIONS
AT THE 1-GeV SYNCHROCYCLOTRON IN PNPI

D.A. Amerkanov, S.A. Artamonov, E.M. Ivanov, J.S. Lebedeva, G.F. Mikheev, G.A. Riabov,
O.A. Shcherbakov, A.S. Vorobyev
in collaboration with the Branch of JSC "United Rocket and Space Corporation" – "Institute of Space
Device Engineering" (Russia): P.A. Chubunov, V.S. Anashin, L.R. Bakirov, A.E Koziukov

1. Introduction

The proton synchrocyclotron SC-1000 with the proton energy of 1 GeV and intensity of the extracted proton beam of 1 μA [1] is one of the basic installations of the PNPI. It was commissioned in 1970 and was significantly modernized during its exploitation. The experimental complex of the SC-1000 is used for investigations in the fields of elementary particle physics, atomic nuclear structure and mechanisms of nuclear reactions, solid state physics, and for purposes of applied physics and nuclear medicine. Radiation resistance testing of electronics is conducted at the SC-1000 during more than two decades. A sharp growth of the needs in the accelerated single-event effect testing of electronic components and systems intended for avionic/space and other applications has led to a development of new test facilities at high-energy accelerators, which are used as powerful sources of protons and neutrons.

In the present report, a short description is presented of the proton (IS SC-1000 and IS OP-1000) and neutron (IS NP/GNEIS) test facilities developed at the PNPI in collaboration with the Branch of JSC "United Rocket and Space Corporation" – "Institute of Space Device Engineering" (Branch of JSC "URSC"– "ISDE"), a Head Organization of the Roscosmos Interagency Testing Centre. A unique conjunction of proton beams with variable energy 60–1 000 MeV and a neutron beam with a broad energy range (1–1 000 MeV) spectrum enables to perform complex testing of semiconductor electronic devices at the SC-1000 within a single testing cycle.

2. Proton test facilities

At present, two of three proton beam lines of the SC-1000 are used for radiation testing of electronics. The IS SC-1000 test facility has a fixed proton energy of 1 000 MeV and is located in the P2 beam line. At the IS OP-1000 facility located at the P3 beam line, the proton energy can be varied from 1 000 MeV down to 60 MeV by means of a system of copper degraders (absorbers) of variable thickness from 73 mm (at 900 MeV) to 530 mm (at 60 MeV) [2]. A scheme of the proton beams and irradiation workstations placed in the experimental room, as well as a photo of the degrader system located in the SC-1000 main room are shown in Fig. 1. The parameters of both proton test facilities are given in Table 1.

An adjustment of the proton beam profile is carried out roughly by means of quadrupole lenses whereas for final tuning a 2m-long steel collimator with 20 mm aperture is used. All irradiations are carried out at open air and room temperature. Both proton and neutron beam lines are equipped with a remotely controlled system intended for positioning the device under test and heating it in the 20–125 °C temperature range.

Parameters of the proton beam at the outlet of the copper absorber of variable thickness were evaluated by means of the GEANT4 code calculation. The energy distribution of the initial proton beam was supposed to be of a Gaussian type with the parameters of 1 000 and 3.84 MeV for the proton energy and standard deviation, respectively. The results of GEANT4 calculations are given in Table 2 and Fig. 2. Both incoming and outcoming proton beam parameters were verified experimentally by means of ToF-measurements carried out using the microstructure of the proton beam (~ 73 ns between proton micropulses).
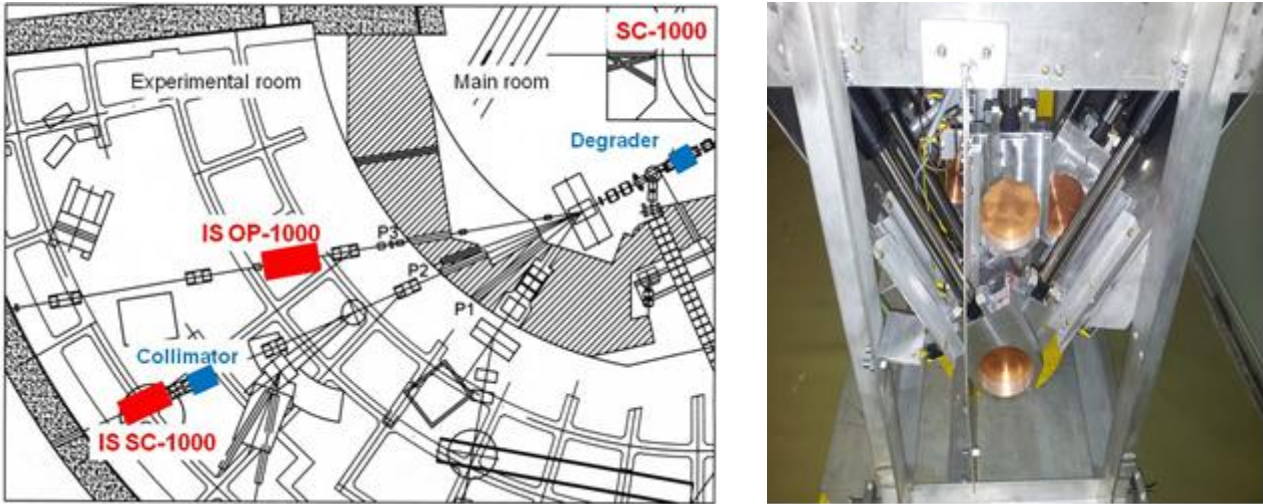
Fig. 1. Scheme of the proton beam lines: P2 – protons with the energy of 1 000 MeV; P3 – protons with the energy variable from 1 000 to 60 MeV (*left*); device for remote variation of the absorber length and of the proton energy (*right*)

Parameters of the proton test facilities

Parameter	IS SC-1000	IS OP-1000
Irradiation conditions	Atmosphere	Atmosphere
Particle	Protons	Protons
Energy, MeV	1 000	60–1 000
Flux, p/cm$^2 \cdot$ s	10^5–10^8	10^5–10^8
Irradiation area, mm	$\varnothing \geq 25$	$\varnothing \geq 25$
Uniformity, %	≤ 10	≤ 10
Status	In operation (since 1998)	In operation (since 2015)

Parameters of the proton beam after transmission through the copper absorber (GEANT4 calculation)

| Proton energy, MeV	Standard deviation, MeV	Absorber thickness, mm	Absorber transmission, %
62.1	28.20	530.5	1.6
100.09	24.63	521.2	2.3
197.93	15.77	490.8	3.4
300.21	12.12	448.7	5.4
399.12	10.24	398.0	8.4
499.24	8.92	340.9	13.5
601.03	7.89	279	22.0
699.88	7.01	213.1	35.6
800.18	6.13	144.3	56
899.85	5.13	73.11	82.1
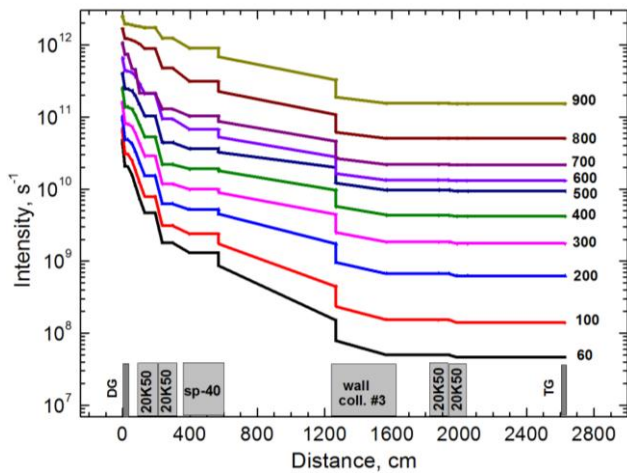
Fig. 2. Dynamics of protons losses at different energies along the beam line P3: DG – absorber; 20K50 – quadrupole; SP-40 – bending magnet; wall, coll. #3 – a wall with the collimator #3 between the main and experimental room of the accelerator; TG – target

The beam diagnostics is carried out using a set of standard tools which includes: 1) a thin scintillator screen coupled with a CCD-sensor for rapid evaluation of the beam profile image, 2) a 2D-moving Se-stripe-type beam profile meter, 3) a double-section ionization chamber for "on-line" control of the proton intensity (fluence), 4) an Al-foil activation technique in conjunction with a high-resolution HPG-detector as an absolute "off-line" monitor of the proton fluence.

3. Neutron test facility

The IS NP/GNEIS test facility is operated since 2010 at the neutron ToF-spectrometer GNEIS [3, 4]. Its main feature is a spallation source with the neutron spectrum resembling that of terrestrial neutrons in the energy range of 1–1 000 MeV. The water-cooled lead target located inside the accelerator vacuum chamber (Fig. 3) produces short 10 ns pulses of fast neutrons with a repetition rate of 45–50 Hz and an average intensity up to $3 \cdot 10^{14}$ $n \cdot s^{-1}$. The IS NP/GNEIS test facility is located inside the GNEIS building on the neutron beam No. 5, which has the following parameters:

- neutron energy range: 1–1 000 MeV,
- neutron flux: $4 \cdot 10^5$ $cm^{-2} \cdot s^{-1}$ (at 36 m flight path),
- beam diameter: 50–100 mm (at 36 m flight path),
- uniformity of the beam profile plateau: ±10%.
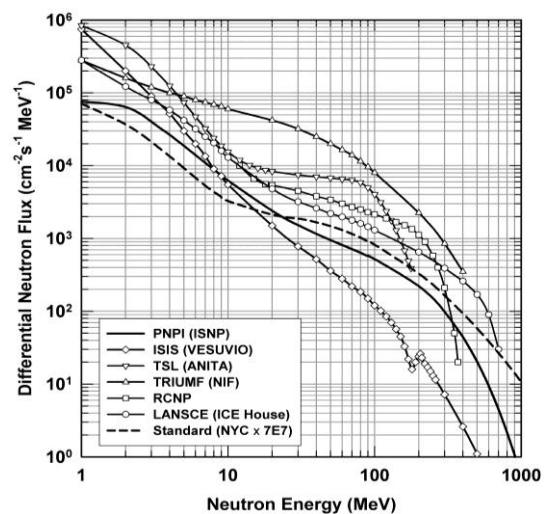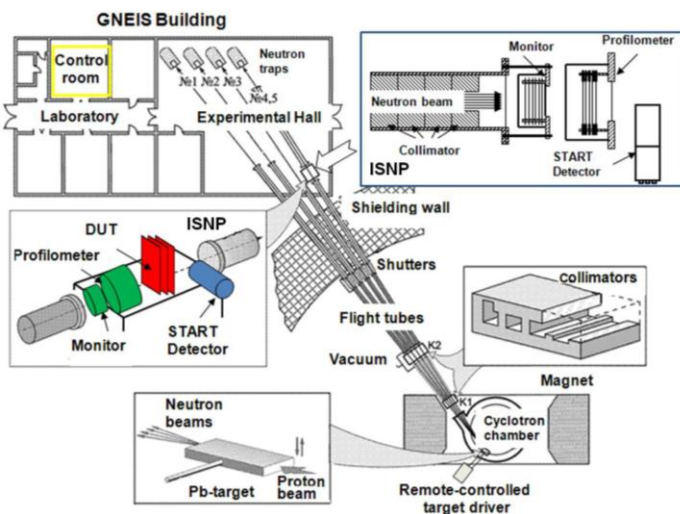
Fig. 3. General layout of the neutron time-of-flight spectrometer GNEIS and IS NP test facility (*left*); neutron spectrum $F_{IS\,NP}(E)$ of the IS NP/GNEIS facility in comparison with the standard terrestrial neutron spectrum and spectra of other world-class test facilities (*right*)

388

The neutron flux of $4 \cdot 10^5$ cm$^{-2} \cdot$ s^{-1} is an integral over the neutron spectrum in the energy range 1–1 000 MeV. It corresponds to the maximum value of 3μA of the internal average proton beam current. The neutron flux and the shape of the neutron spectrum are measured using a neutron monitor and the ToF-technique (Fig. 4). The neutron monitor is a fast parallel-plate ionization chamber which contains two targets of ^{235}U and ^{238}U. The neutron fission cross sections of these nuclei are the recommended standards in the energy range 1–200 MeV. The neutron beam profile is measured by means of a multiwire proportional chamber (MWPC) – a two-coordinate position sensitive MWPC used for registration of fission fragments from the ^{235}U target deposited on the MWPC's cathode [5].
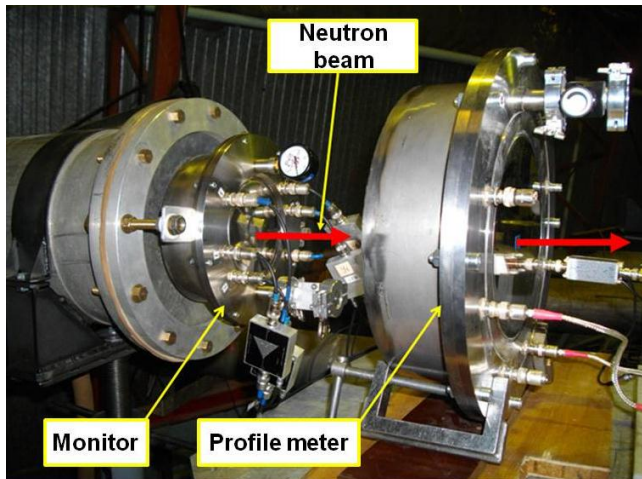

Fig. 4. Neutron monitor and a profile meter MWPC

The neutron spectrum $F_{\text{IS NP}}(E)$ is shown in Fig. 3 together with the JEDEC standard terrestrial neutron spectrum from JESD89A referenced to New York City and multiplied by a scaling factor $7 \cdot 10^7$, as well as the neutron spectra of leading test facilities. Both the shape of the neutron flux and neutron intensity demonstrates that the IS NP/GNEIS is successfully competing with other first-grade test facilities with the atmospheric-like neutron spectrum. The SC-1000 possesses a potential to increase the neutron intensity. A new irradiation station located at a distance of 5–6 m from the neutron-production target operated on the extracted proton beam enables to increase the neutron flux at least by 10 times. Simultaneously, irradiation of bulky equipment is possible.

4. Conclusion

A versatile complex of test facilities has been developed at the SC-1000 accelerator of the PNPI. At present, a growing number of Russian research organizations specialized in radiation testing of the electronics conduct their research on the proton and neutron beams under direct agreements with the PNPI or with the Branch of JSC "URSC"–"ISDE".

Acknowledgment

The authors express their sincere gratitude to all colleagues from the PNPI who participated in the development of the radiation test facilities at the SC-1000 synchrocyclotron.

References

1. N.K. Abrosimov *et al.*, Zh. Tekhn. Fiz. **41**, 1769 (1971).
2. S.A. Artamonov *et al.*, Phys. Part. Nucl. Lett. **14**, No. 1, 188 (2017).
3. N.K. Abrosimov *et al.*, Nucl. Instr. Meth. A **242**, 121 (1985).
4. N.K. Abrosimov *et al.*, Instr. Exp. Tech. **53**, 469 (2010).
5. O.A. Shcherbakov *et al.*, IEEE Trans. Nucl. Sci. **63**, 2152 (2016).

NUMERICAL SIMULATION AND OPTIMIZATION OF THE VARIABLE ENERGY 60–1 000 MeV PROTON BEAMS AT THE PNPI SYNCHROCYCLOTRON FOR TESTING THE RADIATION RESISTANCE OF ELECTRONICS USED FOR NEEDS OF AVIATION AND SPACECRAFT

S.A. Artamonov, D.A. Amerkanov, E.M. Ivanov, G.I. Gorkin, G.A. Riabov, V.A. Tonkikh

1. Introduction

The synchrocyclotron (SC-1000) at PNPI accelerates protons to a fixed energy of 1 000 MeV with an intensity of the extracted beam of 1 μA. The accelerator has an extensive network of proton and π- and μ-meson beams, and a neutron beam [1]. However, to solve a number of problems of fundamental nuclear physics and a variety of applications, there is a need for beams of protons with lower energy. It is desirable to have proton beams of variable energy, which are concentrated in one system. The main method of producing such beams is to decelerate a primary beam by using the mechanism of ionization losses in the material, *i. e.* on the basis of using a degrader. At the time, this method was applied in the Joint Institute of Nuclear Research [2] to obtain a medical beam with 200 MeV from a primary beam of 680 MeV, and, for example, for formation of a beam with variable energy in the cyclotron medical centre, the United States [3].

At PNPI this method was also used previously in experiments to study the elastic *pp* scattering in the energy range 500–1 000 MeV [4] and in measuring the cross sections of a whole group of nuclei [5]. For these purposes, a beam with variable energy from 200 to 1 000 MeV with a relatively small intensity of 10^5–10^6 s^{-1} was developed and implemented [6]. However, many accelerators are used at present not only for solving scientific problems. More and more of their operating time is devoted to practical purposes.

The proton therapy at the SC-1000 with a beam energy of 1 000 MeV (the Gatchina method) gives very good results, but its application is limited to a fairly narrow range of diseases [7]. Therefore, in PNPI a possibility of forming a proton beam with the energy of 140–230 MeV for treatment of patients with oncological diseases of internal organs based on the effect of the Bragg peak was additionally investigated [8]. During the execution of works [4–6, 8], the simplest design of a degrader, which was a set of cylindrical copper disks 80 mm in diameter installed in the guide housing close to each other, was used. The degrader was located close to the output window of the accelerator; its length could be changed manually to produce the required energy.

Recently, a new applied problem has emerged. For successful operation of aviation and space technique in conditions of radiation, radiation-resistant electronics are required. A universal centre for testing electronic components (EC) for the needs of aviation and cosmonautics is being created at the accelerator SC-1000 PNPI jointly with the research Institute of Space Instrumentation. One of the main tools of such tests is the proton beam of variable energy. However, for multiple radiation tests of electronic components, it is necessary to have fast tunable beams with wider energy ranges than the previous ones – ~ 60, 100, 200, 300, 400, 500, 600, 700, 800, 900, and 1 000 MeV, and with a whole set of preassigned properties. In particular, for radiation tests, a higher beam current with a flux density of 10^8 cm^{-2} · s^{-1} and 10% homogeneity area of the beam of at least 25 mm in diameter is needed; it is necessary also to provide a possibility of temperature changes of the test object from +25 to +125 °C. For realization of all these conditions, it is necessary to build a degrader whose length can be changed remotely. Moreover, it is necessary to determine the material from which it is possible to produce the degrader and develop its automated construction. This will allow for each experiment the necessary value of the beam energy to be installed easily and safely, and to reduce significantly the dose load on the staff and unproductive consumption of the accelerator working time. The degrader is preferably positioned as close as possible to the focusing lens to increase the beam intensity at low energies. A complete computer control for the magnetic elements of the designed line should be fulfilled. A permanent test stand to work on the beams with the specified parameters should be built. Ultimately, the process of irradiation of electronic components should be maximally automated.

Time-consuming calculations for each required value of the beam energy were needed to implement such an ambitious program. With the software package GEANT4 [9], Monte Carlo (MC) simulations were performed of the passage of protons with an energy of 1 000 MeV with the desired properties, reflecting

the experimental parameters of the beam through the degraders of copper and tungsten, and the lengths of the degraders for each energy ~ 60, 100, 200, 300, 400, 500, 600, 700, 800, 900, 1 000 MeV were determined. For the specified set of energies, the parameters of the beams which passed through the copper degrader were calculated. The data were used as the input data for the MESON [10] and OPTIMUM [11] programs, which allowed us to trace the trajectory of each proton in the channel, optimize the beam parameters, and determine the optimal modes of all magnetic elements of the line. Thus, the main calculated parameters for each beam, such as intensity, energy heterogeneity, beam sizes, and the homogeneity of its spatial distribution have been obtained.

2. SC-1000 accelerator and the beam lines with variable energy

The intensity of the extracted proton beam with an energy of 1 000 MeV at the SC-1000 can be varied from 10^6 to $6 \cdot 10^{12}$ s^{-1}, and the beam diameter in the focus can be from 5 to 500 mm in the beam lines P2 (medical beam) and P3 (IRIS beam). The versatility of the synchrocyclotron of PNPI is due to the well-developed system of primary and secondary beams, which is shown in Fig. 1 in Ref. [12], where, in particular, the old layout of the equipment placement is presented: degrader, collimators, the parting magnet, two doublets of quadrupole lenses (ML1 and ML2), and the experimental set-up [4, 5] in the direction P3.

For radiation tests of electronic components, it is necessary to have beams of variable energy with the maximum intensity, especially for low values of energy. It is possible to increase the intensity of such beams without significant reworking of the existing line due to proximity of the degrader to the focusing lenses in the main hall of the accelerator. For this purpose, the degrader should be designed to fit into the gap of ~ 90 cm.

Therefore, it was decided to form a new beam of protons of variable energy ~ 60, 100, 200, 300, 400, 500, 600, 700, 800, 900 MeV on the current direction of P3 (1 000 MeV – on the current direction of P2). The alteration of the line is reduced mainly to designing and manufacturing of a new degrader with remote control, located at a new position of this line (see Fig. 1 in Ref. [12]). Three collimators 1, 2, and 3, limiting the size and divergence of the beam, two doublets of quadrupole lenses, and the SP-40 bending magnet remain the same. The total length of the line will be ~ 26 m.

3. Modeling with the GEANT4 software program

One of the most common and widely used codes for calculations of passage of particles through matter, based on the MC method, is the GEANT4 program [9]. In the present work, using this program we generated before the degrader a beam of protons (a few million trajectories) extracted from some vacuum volume of the accelerator line. It was assumed that the beam had a Gaussian form with the parameters $\sigma_x = \sigma_z = 0.64$ cm (x, z are the cross sizes) and the energy of 1 000 MeV ($\sigma_E = 3.84$ MeV), which correspond to the experimental results. Here σ is the standard deviation.

In the simulation of the passage of the beam through the degrader, the set of physical interactions (Physics List) describing the electromagnetic processes, Emstandard_opt3, was applied. The energy loss due to ionization, formation of δ electrons, multiple scattering, Compton scattering, bremsstrahlung, the photoelectric effect, the pair production, and e^+e^- annihilation were taken into account. All hadron interactions (elastic scattering, formation of mesons, decays of particles, excitation of nuclei and emission of photons, nuclear fission, neutron capture, and nuclei disintegration) were also linked up. The interactions described by the class G4InelasticProcess are of special interest in the field of hadronic interactions. Three models for inelastic interactions are provided in the package GEANT4. This is the algorithm GHEISHA, which was also implemented in the previous version of the GEANT3 [13], and the algorithms Bertini cascade and Binary cascade.

3.1. Determination of the material and length of the copper and tungsten alloy degraders

It was assumed in all calculations that the degrader is fabricated in the form of a cylinder 80 mm in diameter either of copper with the density $\rho_m = 8.88$ g/cm^3 or of the alloy of powders: tungsten (T) of 97.50, nickel (N) of 1.75, and iron (I) of 0.75% (TNI) with a density of $\rho_w = 18.6$ g/cm^3.

The length of the degrader for obtaining protons with necessary energy E_i was defined as the difference of the proton ranges, $L_D = R_0 - R_i$, where R_0 is the range of protons with the initial energy $E_0 = 1\,000$ MeV and R_i the range of protons with the energy E_i.

Choosing a degrader made of copper, its degrader length L_{Dm} can be determined using this simple formula. In the case a degrader is made of an alloy of tungsten–nickel–iron powders, the length L_{Dw} of the TNI degrader can be determined also by the same formula.

Table 1 in Ref. [12] presents estimation results for a variant of the degrader made of the alloy of the TNI powders. It also shows for comparison the values of the mean ranges of protons of different energies obtained by the calculations using the well-known SRIM program [14]. It follows from Table 1 in Ref. [12] that the error in the calculation of the length of the degrader L_{Dw} according to the SRIM and GEANT4 for the entire range of energies reaches $\Delta L \approx 2\%$. The length of the degrader, calculated with SRIM, for all values of energies is larger than that determined using the code GEANT4. The experience of previous calculations [6] indicates that the difference of $\Delta L \approx 2\%$ can lead to significant inaccuracies in determination of the given values of energy.

An analysis of the calculation results shows that, taking into account modern possibilities in the manufacture of details by the powder metallurgy method, for each value of the energy, a degrader of the desired length from the TNI alloy can be formed on the basis of a combination of 13 base discs with the diameter of 80 mm. The disks should have the following thickness: 100, 100, 50, 50, 20, 20, 10, 5, 2, 2, 1, 0.5, and 0.3 mm. It was clarified in the process of developing the degrader that the production of the discs made of the TNI alloy with a specified density $\rho_w = 18.6$ g/cm^3 is possible in principle, but only with the use of a quite complex and expensive technology. It was therefore decided, together with the degrader from the TNI alloy, to consider the case where the traditional copper is selected as the material of the degrader. This required new calculations to find the design of the degrader and its collimator made of copper.

The final lengths of the degrader made of copper with the density $\rho_m = 8.88$ g/cm^3, obtained on the basis of calculations using the SRIM, GEANT3, and GEANT4 for different values of energies are presented in Ref. [12] in Table 2. The calculations showed that the technical implementation of the stacked degrader made of copper with $\rho_m = 8.8$ g/cm^3 is quite possible using 11 base disks 80 mm in diameter of the following thicknesses: 200, 150, 100, 50, 20, 20, 10, 5, 2, 2, and 1 mm.

3.2. Beams of variable energy after the copper degrader

In the calculations using the GEANT4 for protons which passed the degrader, the coordinates, the momentum, and the energy of each proton were registered at its output plane, and these parameters were recorded in a separate file for each required level of the beam energy for further multiple analyses. In additional files, information about primary protons (which did not experience inelastic interactions in the degrader) and secondary particles (products of inelastic interactions) was recorded.

The total energy distributions of the protons for different energy values at the exit of the degrader are presented in Ref. [12] in Fig. 2. Table 3 in Ref. [12] presents important results of the calculations for the entire range of energies: a_E – the mathematical expectation of the beam energy; σ_E – the standard deviation; P – the value of the momentum, and the value I/I_0 – the efficiency of the passage of the beam through the degrader in percentage of the intensity of the original beam. These results demonstrate that the magnitudes of the required energies are determined in the calculations reasonably well.

4. Modeling beams of variable energy in the P3 transportation path

One of the objectives of the present work is to calculate and optimize parameters of the beam of a variable energy for tests of radiation resistance of electronic components and to determine optimal operation modes of the magnetic elements of the beam line for all required values of energy. The degrader is a source of particles obtained using the GEANT4 software with a set of parameters that are, for further purposes, the input data for the programs MESON [10] and OPTIMUM [11].

4.1. Methods and algorithms for calculations of the transport channel

The optimized transport channel of the beam P3 consists of two doublets of lenses, a deflection magnet, and a collimator in the wall between the main and experimental halls. The focusing gradients of the magnetic fields in the lenses for obtaining a beam with the maximum intensity and minimum width of the momentum distribution on the target are varied in the optimization. The distance between the lenses in the doublets is not varied because the P3 channel is also used for other purposes.

The MESON program allows us to calculate the parameters of the primary and secondary particle beams by the MC method, which consists of modeling a large number of trajectories of particles passing the given magneto-optical system. The particles of the beam at the entrance to the magneto-optical system are defined in a separate file that contains information about the number of tracks for which the calculation is performed and the parameters characterizing the given particle: the coordinates and the vector components of the momentum, the module of the momentum, and the energy. The file is generated in a special way by the GEANT4 program. The trajectories in free gaps and in the magnetic lenses are calculated by usual formulas [15].

Along with a relatively simple task of the trajectory calculations in the given structure of the tract, the problem of optimizing its parameters should be solved [16]. The optimization problem combines two parts: 1) calculation of the parameters of the beam and 2) the algorithm for searching the optimum. Both of these tasks can be efficiently solved by the MC method.

4.2. Effect of the collimator after degrader on the beam parameters

To improve the beam parameters it was set in the calculations that the new collimator made of copper with the density $\rho_m = 8.88$ g/cm^3 would be located after the degrader. Based on the available practical possibilities for the placement, the collimator was chosen with a length of 132 mm. It was assumed in the calculations that the radius of the hole in the collimator could be varied from $R = 1$ cm to $R = 5$ cm. An analysis of the calculation results shows (see Fig. 3 in Ref. [12]) that the collimator strongly influences the amount of losses for all energy values in the considered range of variation of the radius of the hole.

4.3. Optimal alternation of the polarities of the lenses and the losses during the passage of the transport channel P3

It is commonly accepted that in the channels with a magnet deflecting the beam in the horizontal plane, the polarity of the first doublet HD–HF (horizontal defocusing–horizontal focusing) is chosen to get a small size of the beam after the magnet in the plane of its deflection. This representation was set in the initial calculations with the optimization of the parameters. However, further optimization calculations of the parameters of the channel revealed that the alternation of the polarities HF–HD for the two doublet lenses 20K50 gave for the specific geometry of the considered channel a higher intensity at the end of the path than the opposite polarities. Figure 2 in Ref. [17] presents a typical calculated change of the number of protons with the energy 60–900 MeV after the passage of the transport channel. The results of the optimization show that for all energies there is a significant decrease of the number of protons in the main hall of the accelerator, *i. e.* at the initial part of the tract. This is due to the fact that after the degrader and collimator the emittance of the beam is substantially larger than the acceptance of the channel. A similar situation is

observed with the passage of the proton beam through the deflecting magnet SP-40 and the holes in the wall between the main and the experimental halls, which is a natural collimator with a hole diameter of 110 mm.

4.4. Optimization of the size of the beam for different energies

The optimal gradients of the magnetic fields in the lenses for all values of energies, achieving their maximum possible intensity with the minimum width of the momentum distribution at a target with a diameter of $d = 5$ cm, are presented in Fig. 5 of Ref. [12].

The optimal parameters of beams of different energies with the same diameter $d = 5$ cm of the target are presented in Table 1.

Table 1

Estimated parameters of beams of different energies at the end of the path for the same diameter of the target $d = 5$ cm[*]

E_i, MeV, desired	E_i, MeV, calculated	I, s^{-1}	$\Delta P/P$, %	σ_x, cm	σ_z, cm	Homogeneity 10%	
						x, mm	z, mm
60	62.1	$1.53 \cdot 10^7$	14.9	3.00	1.41	25.9	14.5
100	100.1	$4.60 \cdot 10^7$	12.2	3.63	1.37	35.2	14.7
200	197.9	$2.06 \cdot 10^8$	7.93	2.46	1.37	25.3	17.2
300	300.2	$5.87 \cdot 10^8$	4.70	2.48	1.44	24.0	19.0
400	399.1	$1.39 \cdot 10^9$	3.29	2.26	1.44	24.4	21.0
500	499.2	$3.13 \cdot 10^9$	2.49	2.27	1.38	23.3	21.5
600	601.0	$4.33 \cdot 10^9$	1.96	1.26	1.41	13.6	16.3
700	699.9	$7.23 \cdot 10^9$	1.51	0.86	1.51	12.0	27.0
800	800.2	$1.67 \cdot 10^{10}$	1.27	0.69	1.55	11.3	27.0
900	899.8	$5.10 \cdot 10^{10}$	0.98	0.57	1.48	11.7	19.7

[*] Here ΔP is the full width of the momentum distribution of the beam at the half-maximum (FWHM).

The table results indicate that the requirement of 10% uniformity of beams with the dimension of ≥ 25 mm simultaneously for the two transverse coordinates x and z directions cannot be satisfied with the target of the diameter $d = 5$ cm for all values of energies. Therefore, more research is needed to obtain the necessary transverse beam sizes for the complete set of energies.

For this purpose, the optimization calculations were performed for different possible target diameters from $d = 5$ cm to $d = 18$ cm while maintaining the number of particles that reached the target. The information about the shape of the beam is given by the standard deviations σ_x and σ_z calculated by the specified method for each desired value of the energy.

Figure 6 of Ref. [12] shows how the optimized values of the standard deviations σ_x and σ_z depend on the diameter of the target for the energies of ~ 60, 100, 200, and 300 MeV. It is seen that for all these energies the standard deviation σ_x is a slowly varying function of d, while σ_z has a not predictable behaviour with increase of d.

The values of the gradients of the magnetic fields in the quadrupole lenses of the experimental hall for all values of the energies realizing their maximum possible intensity with the minimum width of the momentum distributions on the targets with the optimal diameters are presented in Fig. 8 of Ref. [12]. The calculation results for all energies are summed in Table 2.

Estimated parameters of beams of different energies at the end of the path for the optimal diameters of the target

d_{opt}, cm	E_i, MeV, calculated	σ_x, cm	σ_z, cm	Homogeneity 10%	
				x, mm	z, mm
15	62.1	2.88	2.84	27.8	27.0
18	100.1	3.40	3.53	31.5	33.9
15	197.9	2.62	3.14	28.1	28.1
18	300.2	3.18	3.41	30.8	30.5
15	399.1	3.01	2.44	35.7	34.0
13	499.2	2.46	2.64	27.3	32.9
15	601.0	2.82	2.71	30.5	34.9
13	699.9	2.49	2.43	31.2	34.0
9	800.2	1.45	1.81	27.1	29.8
11	899.8	2.71	1.78	34.9	30.8

5. Conclusion

At the SC-1000 PNPI, together with the research Institute of Space Instrumentation, a universal centre for testing the electronic component base for aviation and space has been built.

For a successful implementation of this task, careful and time-consuming calculations for each required value of the beam energy were done. Simulations of the passage of protons with an energy of 1 000 MeV through copper and tungsten degraders were performed by the MC method using the GEANT4 software package [9]. As a result, the lengths of these degraders providing the required energies ~ 60, 100, 200, 300, 400, 500, 600, 700, 800, 900, and 1 000 MeV were determined. For the desired set of the energies, by selecting the copper degrader, the parameters of each beam which passed the degrader were calculated. The data were used as the input data for the MESON [10] and OPTIMUM [11] programs, which allowed us to trace the trajectory of each proton in the beam transport line, to choose the optimum size of the collimator of the degrader, to optimize the beam parameters in the channel, and to determine the optimal modes of all the magnetic elements of the tract. The main parameters of each beam, such as the intensity, the energy heterogeneity, the beam sizes, and the homogeneity of its spatial distribution were calculated. The calculations showed a possibility to form beams of protons in the energy range 1 000–62 MeV with the density of the intensity at the place of exposure from $1 \cdot 10^9$ to $6 \cdot 10^5$ cm$^{-2} \cdot$ s^{-1} with the 10% homogeneity area in intensity within a diameter of no less than 25 mm. A copper degrader with a remote change of its length and with a fully automated control system was designed and built. This system allows the necessary value of the beam energy to be installed easily and safely, and it allows one to significantly reduce the dose load on the staff and unproductive consumption of the accelerator working time in each experiment. The degrader was placed as close as possible to the focusing lens channel P3, which resulted in an increase of the beam intensity at low energies. A complete computer control of the magnetic elements of the line was implemented.

In conclusion, it should be emphasized that at the SC-1000 radiation tests of electronic components can be carried out not only in proton beams of variable energy 62–900 and 1 000 MeV, but in the neutron beam with a spectrum similar to the atmosphere neutron spectrum [18]. Thus, the synchrocyclotron PNPI is the only accelerator in Russia where extensive radiation tests of electronic components can be conducted in proton beams in the energy range of 60–900 and 1 000 MeV and in a neutron beam with energies 1–1 000 MeV.

References

1. N.K. Abrosimov, S.P. Dmitriev, V.A. Eliseev *et al.*, in *Proc. of the 7th All-Union Workshop on Charged Particle Accelerators, Dubna, 14–16 Oct., 1980*, **2**, 75–79 (1981).
2. V.P. Dzhelepov, V.I. Komarov, O.V. Savchenko, Med. Radiol. **4**, 54 (1969).
3. E.W. Cascio, J.M. Sisterson, J.B. Flanz, M.S. Wagner, in *Proc. of the IEEE Radiation Effects Data Workshop, 21–25 July, 2003* (IEEE, Piscataway, NJ, 2003).
4. A.A. Vorobyev, A.S. Denisov, Yu.K. Zalite, G.A. Korolev *et al.*, Preprint PhTI-430 (1972).
5. A.A. Kotov, L.A. Vaishnene, V.G. Vovchenko *et al.*, Phys. Rev. C **74**, 034605 (2006).
6. N.K. Abrosimov, E.M. Ivanov, Yu.T. Mironov *et al.*, VANT, Ser. Phyz. Rad. Vozdeistv. Radioelektron. Appar., No. 4, 43 (2003).
7. N.K. Abrossimon, Yu.A. Gavrikov, E.M. Ivanov *et al.*, J. Phys.: Conf. Ser. **41**, 424 (2006).
8. N.K. Abrosimov, E.M. Ivanov, G.A. Ryabov, M.G. Tverskoy, Preprint PNPI-2805 (2009).
9. GEANT4 a Simulation Toolkit, http://geant4.cern.ch/
10. N.K. Abrosimov, V.A. Volchenkov, G.A. Ryabov, in *Proc. of the 4th All-Union Workshop on Charged Particle Accelerators*, **1**, 258–261 (1975).
11. N.K. Abrosimov, V.A. Volchenkov, G.A. Ryabov, in *Proc. of the 6th All-Union Workshop on Charged Particle Accelerators*, **2**, 175–177 (1979).
12. S.A. Artamonov, E.M. Ivanov, N.A. Ivanov *et al.*, Phys. Part. Nucl. Lett., **14**, No. 1, 188 (2017), DOI 10.1134/S1547477117010046.
13. ROOT. Data Analysis Framework, http://root.cern.ch/installing-geant3
14. SRIM – the Stopping and Range of Ions in Matter, http://srim.org
15. G. Vol'nik, *Optics of Charged Particles*, Energoatomizdat, St. Petersburg, 1992.
16. D.M. Kuz'menkov, V.I. Chernetskii, *Algorithms and Programs of Random Search*, Zinatne, Riga, 1969, p. 145.
17. S.A. Artamonov, D.A. Amerkanov, E.M. Ivanov *et al.*, in *Proc. of XXV Russian Particle Accelerator Conf. (RuPAC 2016), St. Petersburg, 21–25 Nov., 2016*, pp. 105–107.
18. O.A. Sherbakov, A.S. Vorobyev, A.M. Gagarski *et al.*, in *Proc. of Int. Conf. on Radiation Effects on Components and Systems (RADECS-2015), Moscow, 14–18 Sept., 2015*, p. 40.

MAGNETIC FIELD OF THE 40–80 MeV H⁻ ISOCHRONOUS CYCLOTRON AT GATCHINA. EXPERIMENTS AND 3D CALCULATIONS

S.A. Artamonov, D.A. Amerkanov, G.I. Gorkin, V.P. Gres, E.M. Ivanov, G.A. Riabov

1. Introduction

The isochronous cyclotron C-80 which is now started up at the PNPI is planned to be used as for applied physics program – for production of medicine isotopes, for therapy of eye melanoma and surface forms of cancer, for radiation resistance tests of electronic components – as well as for fundamental research in nuclear physics, solid state physics and biology. Here we present the final parameters of the magnetic field distribution of the new H⁻ isochronous cyclotron and results of 3D computer calculations and experimental measurements.

The magnet and the magnetic system are the most important and expensive parts of the cyclotron, and a considerable attention was paid to their design. The magnetic field of the cyclotron C-80 should meet several requirements. The magnetic field rigidity at the final orbit must reach Br = 13.2 kGs · m, which corresponds to 80-MeV energy of the proton beam. For insuring the isochronism, the magnetic field averaged over the azimuth when going from the centre of the magnet to the final orbit should increase by ~ 8.5%. The azimuthal variation of the magnetic field should provide the vertical and horizontal transversal focusing. Some room should be left for a high frequency system: the gap between the shims should be wider than 160 mm. In distinction from a standard cyclotron, there is an additional and essential requirement for an H⁻ machine – to keep H⁻ losses due to dissociation less than some percent. Acceleration of H⁻ ions has obvious advantages: a possibility for 100 % extraction of the beam with high intensity and variable energy. On the other hand, it requires a special source of H⁻ ions, high vacuum, and what is most important, the magnetic field strength in the magnet sector should not exceed in our case 16.8 kGs to prevent H⁻ electromagnetic dissociation.

2. General description

A few years ago, as a first approximation, the magnetic structure of the cyclotron was designed on the basis of 2D calculations by using the POISSON program and measurements on two small models [1, 2]. The geometry and the key parameters of the magnetic system for the cyclotron were selected. It was supposed that the height of each of the sectors would be equal to 90 mm, and during further optimization it was not changed. For obtaining the required isochronism, the height of the correction sector shims was varied. The initial height of these shims was selected equal to 20 mm. Besides, in the course of the optimization, a special constrained condition was imposed. It was required that the amplitude of the main fourth field harmonic should not exceed ~ 3 000 Gs, and the field near the extraction radius $r \approx 90$ cm should be $B \leq 16\,800$ Gs. To reduce H⁻ dissociation losses, a magnetic structure of C-80 with high spiral angles was proposed. Under these conditions, the H⁻ dissociation should be below 5% [3]. For these purposes, additional valley shims were introduced into the magnetic system, and their geometrical parameters were also varied. Thus, the formation of the demanded isochronous field was carried out only by changing the iron shims geometry without using correction coils. For an improvement of the accelerated beam orbits centering and reducing lower magnetic field harmonics (1, 2, 3), four pairs of azimuthal correcting coils were installed between the sectors at the radii 85–1 025 mm.

The extraction of the beam of variable energy 40–80 MeV in the H⁻ isochronous C-80 cyclotron is performed without variation of the magnetic field but by changing the radial position of the stripping foil.

The major unit of the cyclotron, its electromagnet, was designed using the model of the magnet of the PNPI SC-1000 synchrocyclotron (SP-72). This electromagnet has a traditional design with an E-shaped magnet yoke and a pole of 2.05 m in diameter. The system to move upward the magnet upper part (the half-yoke) was worn-out and outdated. Therefore, it was replaced with four pairs of ball bearings and screws equipped with servomechanisms and position sensors. The maximum height of the half-yoke lifting is about 600 mm, the setting accuracy is better than 50 μm.

Main parameters of the C-80 magnetic structure are presented in Table.

Main magnet parameters

Parameter	Value
Pole diameter	2.05 m
Valley gap	386 mm
Hill gap (min)	163 mm
Number of sectors	4
Spiral angle (max)	65°
Field in the centre	1.352 T
Flutter (max)	0.025
Ampere-turns	$3.4 \cdot 10^5$
Power	120 kW
Weight	250 t

3. 3D optimization

The main parameters of the cyclotron magnetic system were refined and optimized by computer simulations with the 3D MERMAID code [4, 5], and the dynamics simulations were performed with the code in Ref. [6]. The main peculiarities and modifications of the preliminary design can be formulated as follows.

The detailed 3D geometry of the magnet yoke, of the sectors (four pairs), sector shims (17 correction shims in each sector), and the valley shims, the coils, and the external boundaries was introduced in the computer model. Because of a big angular extension of the spiral sectors in C-80, it was necessary to use in the calculations a half of the magnet with the corresponding symmetry boundary conditions. The external boundary of the area where the calculations were performed was chosen rather far to get rid of its influence on the magnetic field in the working region and to determine correctly the fringe field. The fringe field was taken into account for correct calculations of the extraction beam optics. Thus, for the description of the magnetic structure of C-80 using the MERMAID program, about 20.5 million direct prisms were required, which allowed to reach the necessary precision of 10^{-3}–10^{-4} in the calculations of the magnetic field.

The nonlinear magnetic properties of the used electro technical steels (three types) were taken into account. To increase the vertical focusing in the central region, the zero and low spiral sectors were prolonged from the radius of 27 cm to the radius of 40 cm.

In the preliminary version of the magnet structure, four valley shims in each valley were used to provide isochronisms on the last radii. To cut down the number of the valley shims from four to one, the azimuthal width of the sectors was expanded by ~ 20 mm from the radius of 70 cm to the final radius of 102.5 cm. Under these conditions, the H⁻ dissociation is below 3 % [5].

Only the 3D field calculations made possible to perform the central region design taking into account the axial injection system geometry and the design of the magnetic field bump for the beam focusing at the first turns.

4. Main results

At the final stage of the magnetic field formation, the computer calculations and the magnetic field measurements were performed in parallel. The magnetic field in the full scale magnet was measured using a system based on twenty nuclear magnetic resonance calibrated Hall probes and an automated coordinate system, which could position probes in the cylindrical coordinate system with an accuracy of 0.1 mm along the radius at each azimuthal angle (with steps 0.5, 1, 1.5, 2, or 2.5°) at the radii from zero up to 100 cm (with steps 0.5, 1, 1.5, 2, or 2.5 cm). The total measurement accuracy was about 0.02%. The time of the magnet

topography measurements on the super period was ~ 6–8 h and on the periodicity element was about 2 h. The local field defects were corrected by using iron shims. The necessary shim thickness was estimated by 3D calculations. Disagreements between the computer predicted and the measured fields did not exceed some Gs.

The final field distribution (Fig. 1) was reached by selection of the thickness of the 17 types of the iron sector shims in every sector and selection of the thickness of the valley shims by using the trial-and-error method.
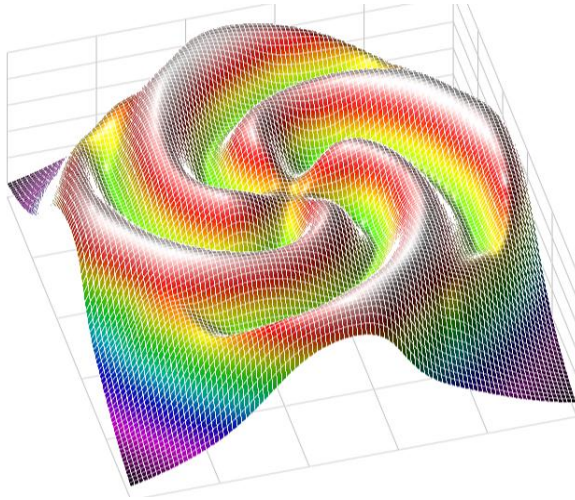
Fig. 1. Final magnetic field distribution

As a result, the magnetic field was obtained which provided the beam acceleration from the radius of ~ 15 mm up to the radius of ~ 90 cm.

We remind that in the working magnet gap four pairs of sectors with high spirality angles were placed. Coils for the correction of the average magnetic field were not used in the cyclotron C-80. For improvement of the accelerated beam orbits centering, four pairs of azimuthal correcting coils between the sectors were installed at the radii 85–1 025 mm.

The comparison of the measured average magnetic field and its isochronous value is shown in Fig. 2.
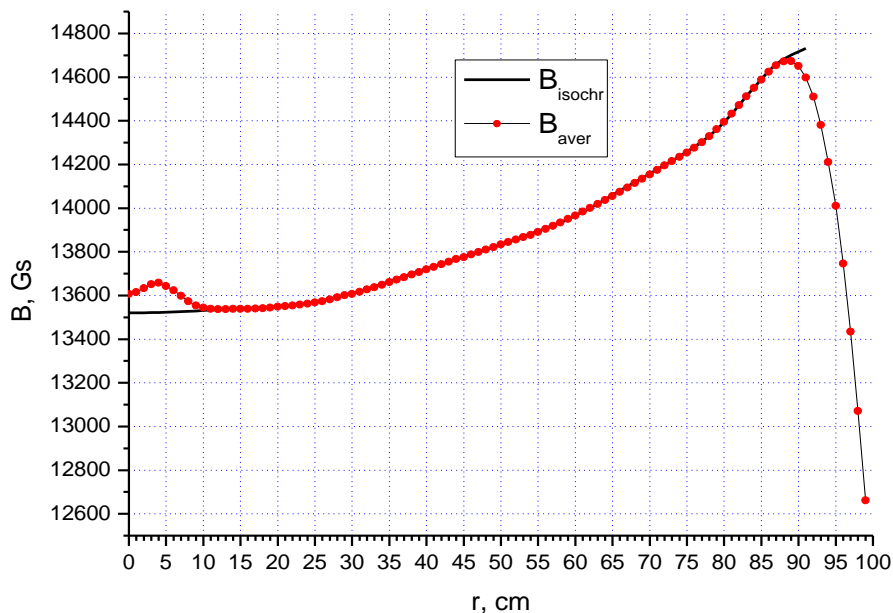
Fig. 2. Comparison of the measured magnetic field B_{aver} and the isochronous field B_{isochr}

The isochronism of the magnetic field was provided with the accuracy of 2–5 Gs. The difference between the measured magnetic field and the isochronous cyclotron field is presented in Fig. 3.
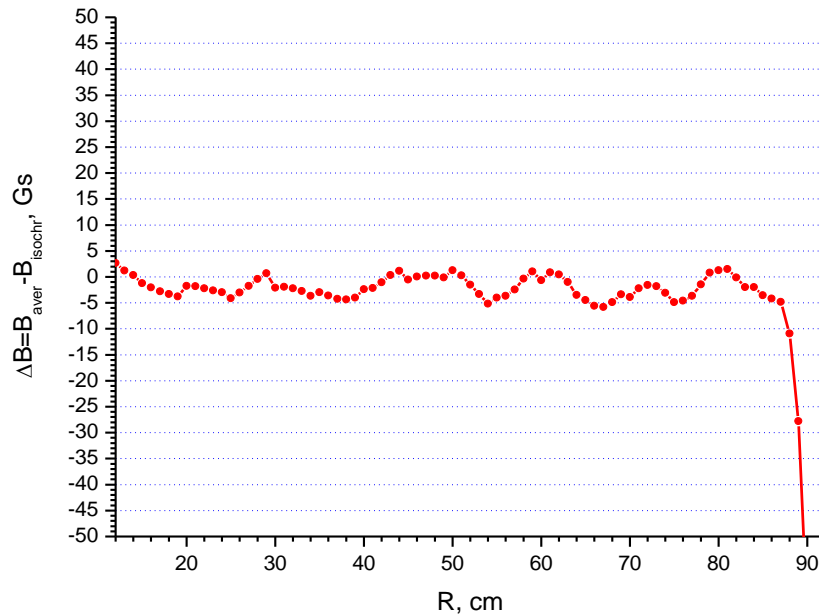
Fig. 3. Difference between the measured magnetic field and the isochronous cyclotron field

The measured harmonics of the magnetic field versus the radius are shown in Fig. 4. It is seen that at the interface of the direct sector with its spiral part, there is a significant decrease of the main harmonic A_4. Near the extraction radii, a growth of the harmonic A_{12} is observed, which hinders the drop of the harmonic A_4.
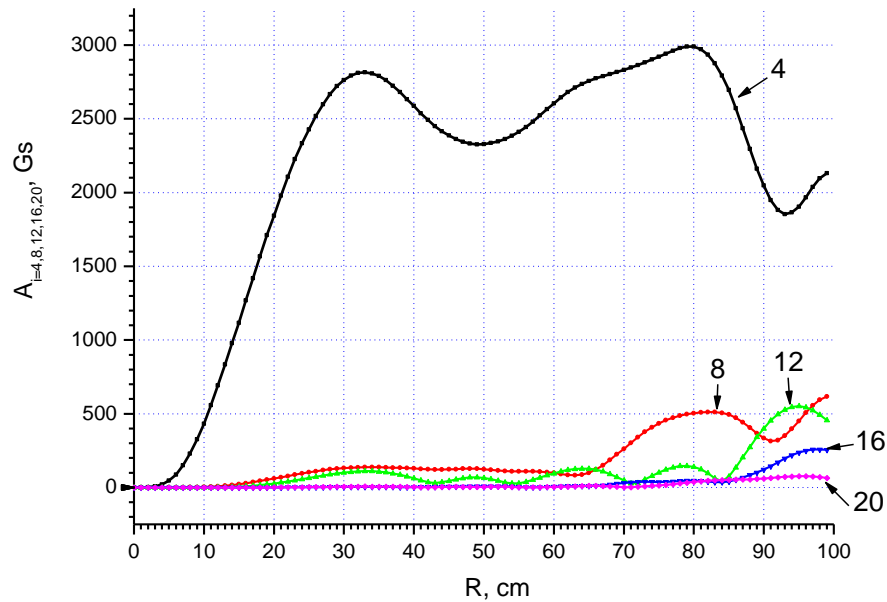
Fig. 4. Measured harmonics (4, 8, 12, 16, and 20) of the magnetic field versus the radius

A special attention was paid to reduce the lower harmonics (Fig. 5). The most dangerous harmonics A_1, A_2, A_3 lead to strong distortions of the accelerated orbits. After considerable efforts in our case, the first harmonic on the last radii did not exceed 10–12 Gs.
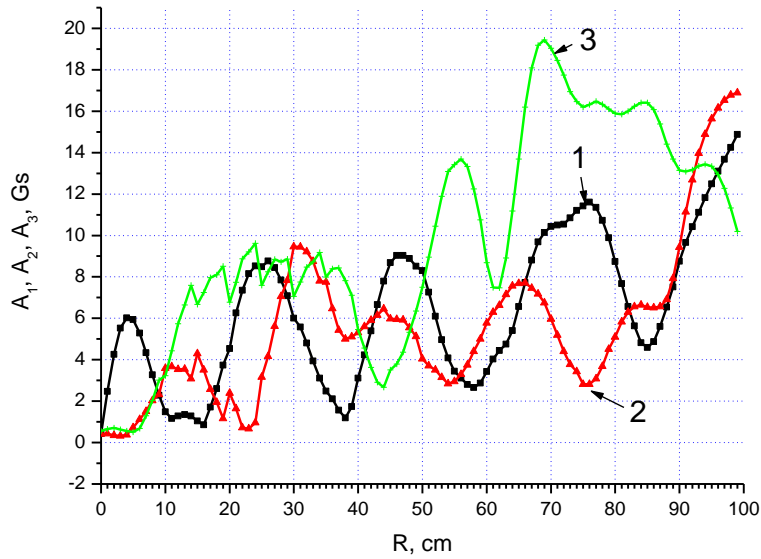
Fig. 5. Measured lower harmonics of the magnetic field versus the radius

The first and second harmonics of the magnetic field perturbations have an essential influence on the radial motion of the beam in C-80. The amplitude of the first harmonic is determined by inaccuracies in production and assembling of the cyclotron magnet. The amplitude of the second harmonic at the last radii is less than 8 Gs.

The nature of the action of these harmonics on the beam dynamics is various. The amplitude of the first harmonic noticeably affects the coherent radial oscillations of the beam, since betathron frequency ν_r in the entire acceleration region is close to 1.

The gradient of the increase of the amplitude of the second harmonic is the driving term of the parametric resonance $2\nu_r = 2$. In principle, this resonance can lead to an increase of free radial incoherent oscillations of the ions and also to a growth of the radial emittance. The effective force of this resonance depends on specific conditions: the value of the gradient, how far the working point is located from the resonance, and the duration of the resonance action.

The first, second, and third harmonics can be compensated only by harmonic coils. In the every valley A, B, C, and D there are four types of the correction coils I, II, III, IV (Fig. 6). The magnetic fields of these four harmonic coils was measured and examined. These coils are used to decrease the lower harmonics A_1, A_2, A_3 of the cyclotron magnetic field. The contributions of the harmonic coils magnetic fields into the measured average field of the cyclotron are presented in Fig. 7.
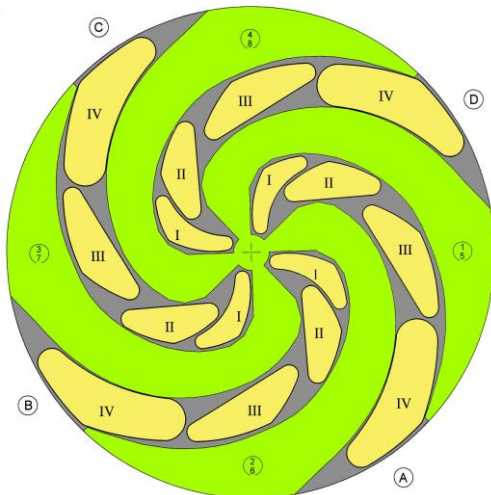
Fig. 6. Top view of the pole tip of C-80
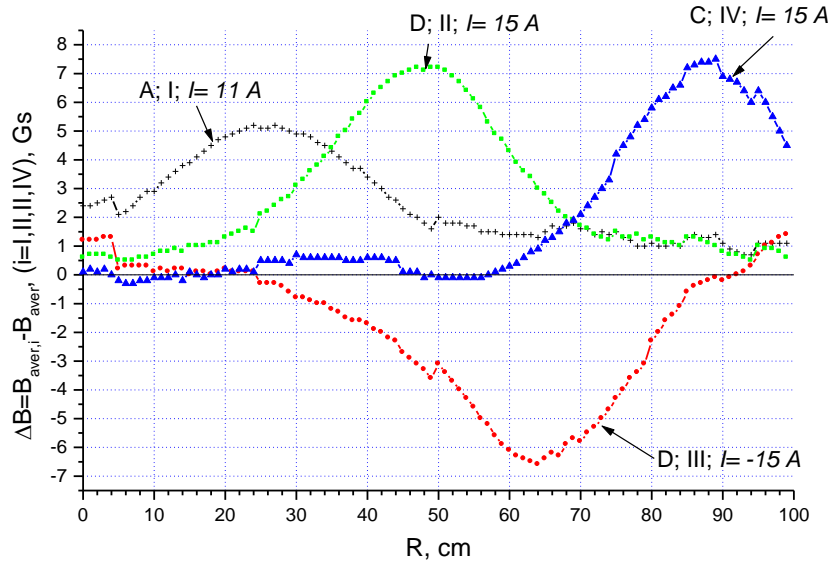
Fig. 7. Contributions of the harmonic coil magnetic fields into the measured average field of the cyclotron

The nominal currents in the harmonic coils were selected as follows: $I - I = \pm 25$ A, $II - I = \pm 25$ A, $III - I = \pm 25$ A, $IV - I = \pm 42$ A.

The measured magnetic field allows the vertical and horizontal focusing (Fig. 8) and the isochronism in the acceleration region [7].
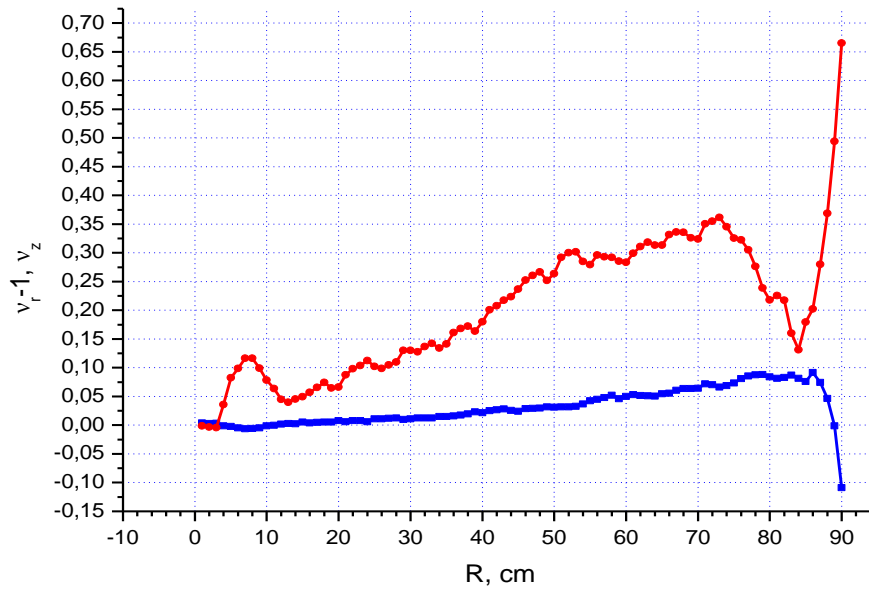
Fig. 8. Frequency of free oscillations ν_r (*blue*) and ν_z (*red*) versus the average radius of the orbit

A special attention was paid to avoid dangerous resonances. Detailed dynamics simulations were performed to be sure that the resonances which are crossed during the acceleration do not cause a significant harmful effect on the beam. The number of ion turns in C-80 is expected to be about 400.

5. Conclusion

Results of the final magnetic field distribution of the 80 MeV H⁻ isochronous cyclotron at Gatchina are presented. Main features and problems are connected with applying the high spirality magnetic structure for acceleration of H⁻ ions. The formed structure permits to accelerate H⁻ ions up to an energy 80 MeV using a rather small two-meter magnet, the beam losses due to the ion dissociation being less than 3%. As far as H⁻ cyclotron operates at the fixed magnetic field, the necessary field distribution was obtained by using iron correction shims only. To obtain the necessary field distribution, 3D-computer calculations and successive magnetic measurements were very helpful.

At the present time, all cyclotron systems are installed and tested. In June 2016, a physical start-up of the C-80 cyclotron system was realized. Works were carried out in the pulse mode at low currents of the accelerated beam to exclude strong activation of the equipment to make possible a safe continuation of works in the cyclotron vacuum chamber, with the components of the beam transport system, *etc*. The design parameters of the cyclotron were obtained in November 2016.

References

1. N.K. Abrossimov, S.A. Artamonov, V.A. Eliseev, G.A. Riabov, in *Proc. of the Second Int. Workshop: Beam Dynamics & Optimization – BDO, St. Petersburg, 1995*, pp. 7–15.
2. N.K. Abrossimov, S.A. Artamonov, V.A. Eliseev, G.A. Riabov, in *Proc. of the XV Int. Conf. on Cyclotron and Their Application, Caen, France, 1998*, pp. 518–521.
3. N.K. Abrossimov, S.A. Artamonov, V.A. Eliseev, G.A. Riabov, *PNPI Research Report 1994–1995*, Gatchina, 1996, pp. 275–278.
4. S.N. Andrianov, S.A. Artamonov, A.N. Dubrovin, V.A. Eliseev, Vestnik SPbSU, Ser. **10**, Iss. 3, 12 (2008).
5. S.A. Artamonov, E.M. Ivanov, G.A. Riabov, N.A. Chernov. in *Proc. of RuPAC 2012, St. Petersburg, 2012*, WEPPC015, pp. 475–477.
6. S.N. Andrianov, S.A. Artamonov, Vestnik SPbSU, Ser. **10**, Iss. 2, 3 (2009).
7. S.A. Artamonov *et al.*, in *Proc. of XX Int. Conf. Beam Dynamics & Optimization, BDO-2014, St. Petersburg, 2014*, pp. 18–19.

HIGH EFFICIENCY STRIPPING EXTRACTION
IN THE 80-MeV H⁻ ISOCHRONOUS CYCLOTRON AT PNPI

S.A. Artamonov, A.N. Chernov, E.M. Ivanov, G.A. Riabov, V.A. Tonkikh

1. Introduction

The start up of a new high intensity isochronous cyclotron with the design beam energy from 40 up to 80 MeV and beam current of 100 µA was announced in November 2016. The cyclotron is intended for production of high quality medicine isotopes, organization of eye melanoma treatment facility, treatment of surface forms of cancer and radiation resistance tests of the electronics for the aviation and space research [1].

The H⁻ cyclotron has the advantage that the high intensity internal beam can be extracted from the acceleration chamber with practically 100% efficiency by transformation of H⁻ ions into H⁺ ions by using a thin foil. The extraction system consists of a probe with a stripping foil, an extraction window in the vacuum chamber and two aligning magnets to match the extracted beam with the beam transport line. The beam optics calculations in the measured magnetic field make it possible to find the optimal relative position of the extraction system elements as well the parameters of the extracted beam with the energy 40–80 MeV. At present, the beam is extracted from the chamber with the efficiency about 100% and there is good agreement with the optic calculations.

The external view of the cyclotron and the first part of the beam transport line are presented in Fig. 1. Basic parameters of the cyclotron are summarized in Table 1.

Fig. 1. The external view of the C-80 cyclotron and the beginning part of the transport line

Table 1

Characteristics of the C-80 cyclotron

Parameter	Value
Magnet	
Pole diameter	2.05 m
Valley gap	386 mm
Hill gap (min)	163 mm
Number of sectors	4
Spiral angle (max)	65°
Magnetic field in the centre	1.352 T
Flatter (max)	0.025
Extraction radius	0.65–0.90 m
Extracted beams	
Energy	40–80 MeV
Method	Stripping

A 3D sketch of the cyclotron and the extraction system are presented in Fig. 2. A schematic view of the extraction system is presented in Fig. 3.
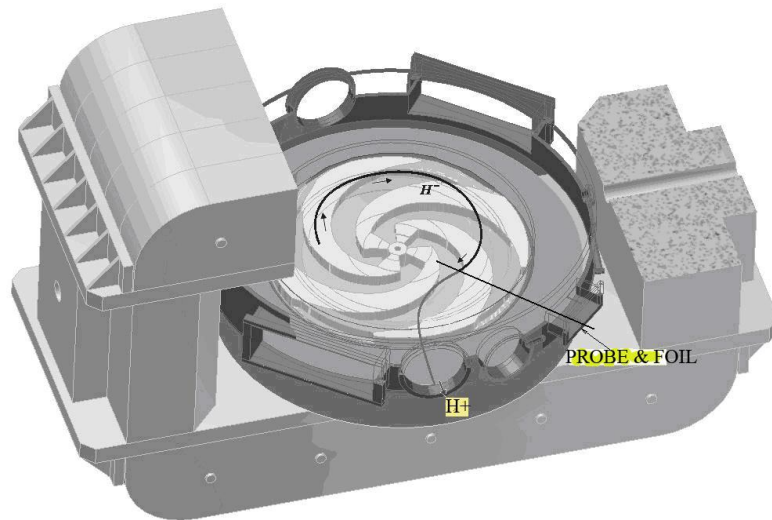
Fig. 2. 3D sketch of the C-80 cyclotron and the extraction system

1 - 40 МэВ
2 - 50 МэВ
3 - 60 МэВ
4 - 70 МэВ
5 - 75 МэВ
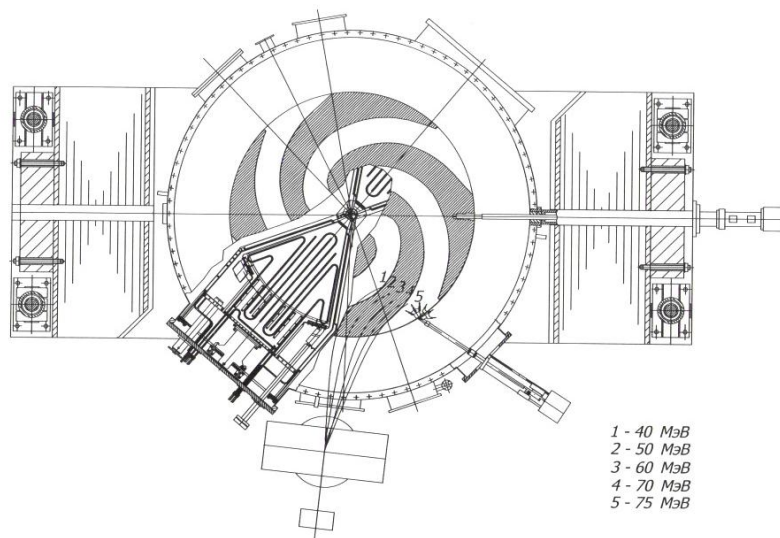
Fig. 3. Schematic view of the extraction system of the C-80 cyclotron

2. Magnetic field

To design the extraction system, it is necessary to know the magnetic field as in the acceleration region, so on the edges. For that reason, the residual magnetic field was measured up to the radius of 230 cm.

The C-80 cyclotron has some specific features in the magnetic structure. As can be seen from Table 1, the magnetic structure with very low flatter and very high spiral angles (up to 65°) is used in the cyclotron. Such a structure makes it possible to decrease the magnetic field in the hill region to avoid beam losses due to electro-dissociation of H⁻ ions. As a result, it permits acceleration of H⁻ ions up to an energy of 80 MeV using a magnet with the pole diameter of 2 m and keeping the beam losses below 3%. A detailed description of the magnetic structure can be found in RUPAC-2014 report [2]. The final magnetic field of the C-80 cyclotron is presented in Fig. 4.
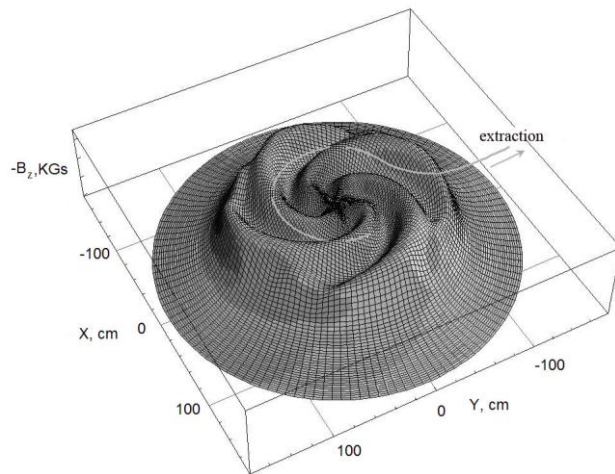
Fig. 4. Magnetic field of the C-80 cyclotron

3. Reference trajectories

One of the problems in designing of the extraction system is to determine the relative positions of the stripping foil and the extraction window in the vacuum chamber. As a first approximation, the positions of the foil and the window were estimated on the basis of simulated closed orbits in the calculated magnetic field. The particle trajectories started from the closed orbits. It was necessary to provide that the participles of different energies pass throw the extraction window and enter the entrance of the aligning magnet. This was achieved by varying the stripper position along the radius and azimuth. Trajectories of the extracted particles are shown in Fig. 5.
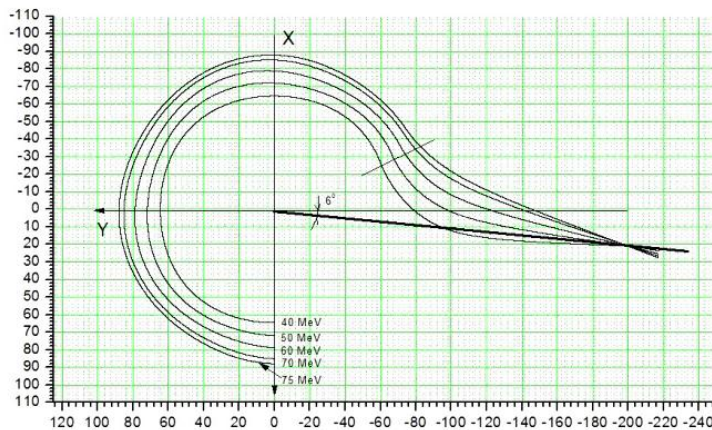
Fig. 5. Trajectories of the extracted particles

As a result of these calculations, it was established that the full energy in a range from 40 up to 80 MeV can be obtained when the stripper foil is moved along a nearly straight line in the coordinate system shown in Fig. 5 (the line equation is $y = 0.88857x - 36.27$). The maximal deviation from the straight line does not exceed a few centimeters.

An original stripper probe with three stripper foils was designed for the C-80 cyclotron. The probe can be moved along the straight line, and in addition each foil can move along the azimuth by 5 cm. As a result, it permits to obtain the whole energy range by moving the probe along the straight line. The reference trajectory calculations made possible to estimate the main parameters of the extraction system: the position of the extraction window in the vacuum chamber, the position and movement ranges of the stripper foil, the arrival points of particles with different energies at the aligning magnet entrance, the direction of the extracted beam and the necessary angle range for the aligning magnet. The direction of the extracted beam is ~ 6° with respect to the longitudinal axis of the cyclotron magnet as it is shown in Fig. 5. The deviation angle in the aligning magnet is varied from 15 up to –4°.

4. Beam optics calculation

Besides the reference trajectory, it was necessary to determine the size and divergence of the beam near the reference trajectory to design the beam transport line.

The computer simulations [3] were used to determine both the reference trajectory and the beam optics. In the linear approximation, the movements in the vertical and horizontal planes are independent, and the beam behaviour can be described by two independent phase ellipses. The starting ellipse size at the stripper in the vertical plane is defined assuming that the maximum beam size in the cyclotron is about 6 mm. The divergence and orientation of the ellipse in the phase space of the vertical plane repeat these parameters of the matched with the magnetic structure ellipse at the radius and azimuth of the stripper. The beam spot at the stripper is supposed to be 3 mm in the horizontal plane and the divergence and orientation of the phase space ellipse corresponds to the matched ellipse. An example of evolution of the phase ellipses in the extraction process for 70-MeV beam is shown in Fig. 6.
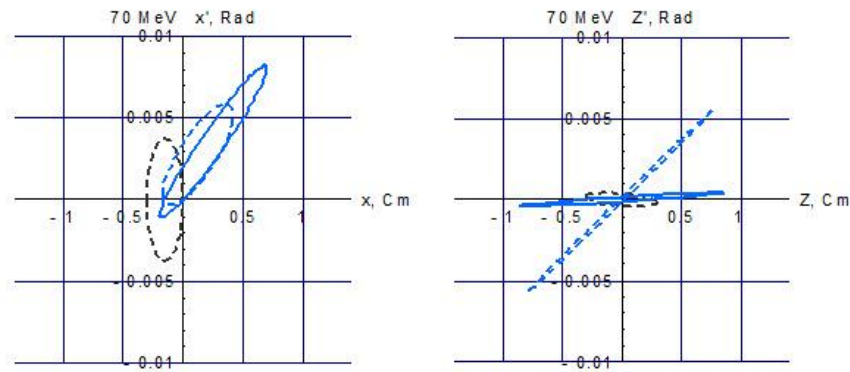
Fig. 6. Phase ellipses for 70-MeV beam in the extraction process: the *black dotted line* corresponds to the stripper position; the *blue dotted line* corresponds to the entrance of the aligning magnet and the *blue solid line* corresponds to the exit of the magnet

Figure 7 shows the evolution of the beam envelopes from the stripper foil up to the exit of the aligning magnet for the 70-MeV beam. After the stripper foil, the beam is exposed to defocusing forces in the horizontal and vertical planes.
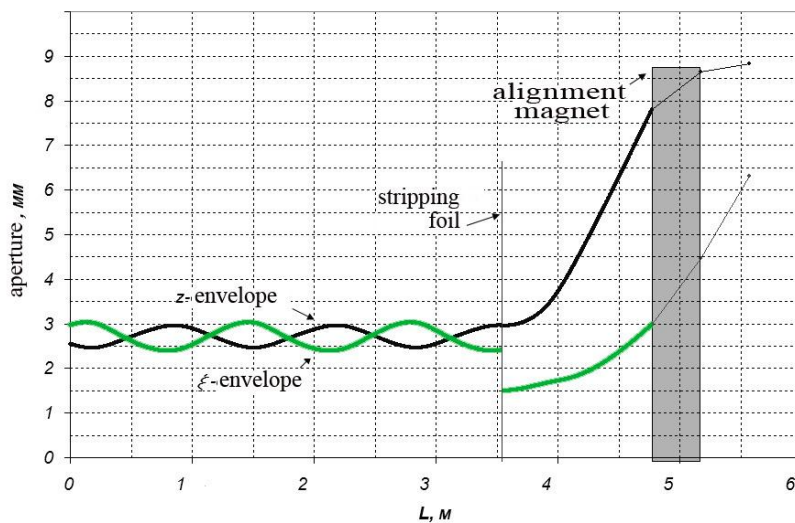
Fig. 7. Transformation of the beam envelopes in the extraction process

The calculated parameters of the beam ellipses at the aligning magnet are presented in Table 2.

Table 2

Twiss beam ellipse parameters at the alignment magnet entrance[*]

T, MeV	40		70	
	ξ	z	ξ	z
α	−1.793	−5.079	−3.562	−3.123
β, mm/mrad	5.801	5.010	3.559	62.220
γ, mrad/mm	0.727	5.348	3.845	0.173
ε, mm · mrad	5.4	3.8	5.6	1.2
D, cm	105		51	
D^1, rad	1.03		0.52	

[*] For details see Ref. [3].

5. Trajectory calculations in the experimentally measured magnetic field

At the final stage, 500 particle trajectories were calculated with random start conditions in the experimentally measured magnetic field map from the inflector exit up to the entrance of the aligning magnet. These calculations confirmed to a great extent the previous results for the positions of the stripper foil and the extraction window, the direction of the extracted beam and the beam parameters. In addition, it was found that the beam spot in the horizontal plane on the stripper foil is 3 mm, as it was assumed in the previous calculations. The energy uncertainty is about 1%. Furthermore, it was found that the internal beam quality strongly depends on the cyclotron tuning, in particular on the central optics tuning, and on the first and third harmonics of the magnetic field. It is interesting to note that the second and fifth harmonics have no effect on the beam emittance.

6. Experiment

The physical start up of the C-80 cyclotron was in summer of 2016. The design beam parameters were achieved in November 2016. The extracted beam was obtained in the energy range from 40 up to 78 MeV. The extraction efficiency estimated as a ratio of the current on the first in beam line Faraday cup and the current on the internal probe was 80–100%. The beam was directed into the beam line, which position was defined from computer simulations. The beam energy could be changed by moving the stripper probe along the calculated line. The results of computer simulations were confirmed by experiment.

Optimization of the beam line and the tuning of the cyclotron regime are planned for the near future.

Acknowledgment

References

1. Yu.N. Gavrish *et al*., in *Proc. of XXV Russ. Particle Accelerator Conf. (RuPAC 2016), St. Petersburg, 21–25 Nov., 2016*, TUCASH04, pp. 176–178.
2. S.A. Artamonov *et al*., in *Proc. of XX Int. Conf. Beam Dynamics & Optimization, BDO-2014, St. Petersburg, 30 June – 04 July, 2014*, pp. 18–19.
3. N.K. Abrossimov *et al*., Preprint PNPI-2851 (2010).
4. N.K. Abrossimov *et al*., Preprint PNPI-2858 (2011).

DEVELOPMENT OF NEW METHODS FOR PRODUCTION OF MEDICAL RADIONUCLIDES AT THE RADIOISOTOPE COMPLEX RIC-80

V.N. Panteleev, A.E. Barzakh, L.Kh. Batist, D.V. Fedorov, V.S. Ivanov, S.A. Krotov, P.L. Molkanov, S.Yu. Orlov, M.D. Seliverstov, Yu.M. Volkov

1. Introduction

The development of nuclear physics experimental methods combined with the use of high current cyclotrons and very sensitive detectors provide very good opportunities for a completely new direction in medical diagnostics and therapies of various diseases. The nuclear medicine technologies used for diagnostics and therapy are based on the employment of artificially produced radioactive isotopes with specific properties. In this paper, the new installation RIC-80 (radioactive isotopes at cyclotron C-80) [1, 2] is shortly discussed, which is being constructed presently at the beam of a new C-80 cyclotron [3]. The RIC-80 project includes the construction of three target stations, one of them is the station coupled with a mass-separator. It is planned to produce the most widely used medical radioisotopes. These are $^{64, 67}$Cu, ^{68}Ge, ^{82}Sr, ^{111}In, ^{123,124}I, $^{223, 224}$Ra, and others, which are under discussion at present as perspective radionuclides for diagnostics and therapy. The mass-separator method will make it possible to produce very pure beams of some radioisotopes.

In this paper, the results on the development of a new method [4] of a high temperature separation of radioisotopes ^{82}Sr and ^{67}Cu and others from different kind of target materials are presented. The production of radionuclides that decay with emission of positrons, allowing their use for positron emission tomography (PET), is very important for diagnostics of different diseases. The isotope-generator ^{82}Sr, which is utilized for PET diagnostics of heart and brain diseases, is one of the most needed radionuclides for PET diagnostics over the world.

The radioisotope ^{67}Cu is regarded now as one of very promising radionuclides for the cancer therapy using monoclonal antibodies. A high demand in radiopharmaceuticals on the base of ^{67}Cu requires new efficient methods for its production, which are actively developed at accelerators.

2. The RIC-80 istallation

The main parameters of the new built C-80 cyclotron are the following: the proton beam energy can be varied in the interval 40–80 MeV, and the beam intensity is planned to be up to 200 μA. The cyclotron is intended mainly for production of a wide spectrum of medical radionuclides for diagnostics and therapy. A photograph of the C-80 external beam line with three proton beam lines to the target stations is presented in Fig. 1. The proton beam line is directed from the ground floor to the cellar, where it can be deflected and focused to one of three target stations. The mass-separator with its target station [2] will allow for production of separated beams of medical radionuclides of a high purity implanted into the corresponding collectors from which they can be easily extracted. The target stations will be equipped with special devices to transfer the highly radioactive targets into protection containers, so that they can be transported safely to special storage places, or to hot cells for the after-treatment and corresponding preparations for pharmaceutics. As it was pointed out previously, the C-80 gives a possibility to obtain sources of a high activity practically for a whole list of radionuclides produced at accelerators.
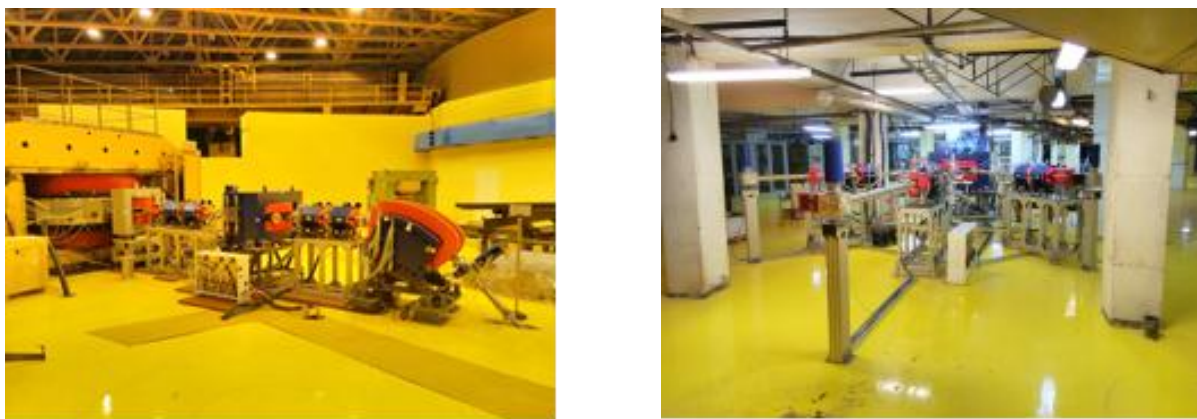
Fig. 1. Cyclotron C-80 (ground floor) with three proton beam lines to the target stations (in the cellar)

3. ^{82}Sr production and extraction from RbCl target material

In the experimental tests for production of ^{82}Sr, the powder of RbCl was used as a target material. The radionuclide ^{82}Sr with a half-live $T_{1/2} = 25.55$ days is a generator for its daughter isotope ^{82}Rb ($T_{1/2} = 1.25$ min), which is widely used in PET diagnostics. For separation of the target material and the produced strontium isotopes, a new developed high temperature method was utilized [4].

After irradiation by a 1-GeV proton beam at the PNPI synchrocyclotron, the RbCl powder was placed into a vessel manufactured from stainless steel, which was put into a Ta–W oven heated by direct current. The powder was heated slowly in a high vacuum to a temperature of 900 °C to be evaporated into a separate volume specially constructed to minimize losses of the irradiated material in the process of its evaporation. At that temperature, the process of complete evaporation of the target material of one gram mass takes about one hour. To control the evaporation process, the γ spectrum of the vessel with the irradiated RbCl was measured at regular intervals [5]. Additionally, after each heating the vessel was weighed to control the mass of the evaporated material. In Figures 2 and 3 a part of γ spectra of the irradiated sample of rubidium chlorine is presented. They were measured with a high purity germanium detector. The γ line of the energy 552 keV belongs to the decay of ^{83}Rb with the half-life 86.2 days and its decreasing indicates the efficiency of the target material evaporation. The γ line of the energy 776 keV belongs to the decay of ^{82}Rb with the half-life 1.27 min, which is the daughter isotope of ^{82}Sr, and its decreasing indicates the strontium radionuclide evaporation. In Figure 2, the spectrum of the vessel with the irradiated RbCl before heating is shown by squares. The spectrum after one hour vessel heating at a temperature of 500 °C is shown by circles. In Figure 3, the spectra after heating at a temperature 500 °C (*red dots*) and at a temperature 900 °C (*green dots*) are compared.

As one can see in Fig. 2, heating of the irradiated sample at a temperature 500 °C for one hour does not give any effect on the target material evaporation. The same result was obtained by weighing the sample before and after its heating at 500 °C. At the same time, Fig. 3 shows that after the vessel with the RbCl was heated up to 900 °C, the target material was evaporated completely with almost hundred percent conservation of strontium. The fact of complete evaporation of the irradiated target material was confirmed by weighing the sample before and after its heating at 900 °C. Finally, the conserved radioactive Sr atoms can be evaporated from the vessel at a higher temperature, or it can be washed out by a small amount of an acid solution.
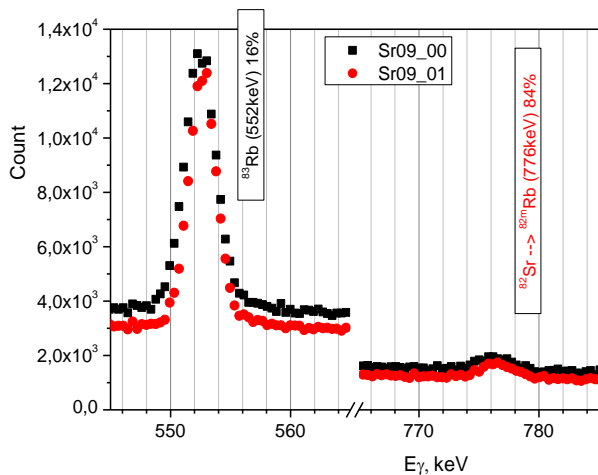
Fig. 2. *On the left* – the spectrum of the vessel with the irradiated RbCl before heating is shown by *squares*; the spectrum after one hour vessel heating at a temperature 500 °C is shown by *circles*. *On the right* – the vessel with the irradiated RbCl powder after one hour vessel heating at a temperature 500 °C is shown [5]. The RbCl white powder is seen in the vessel
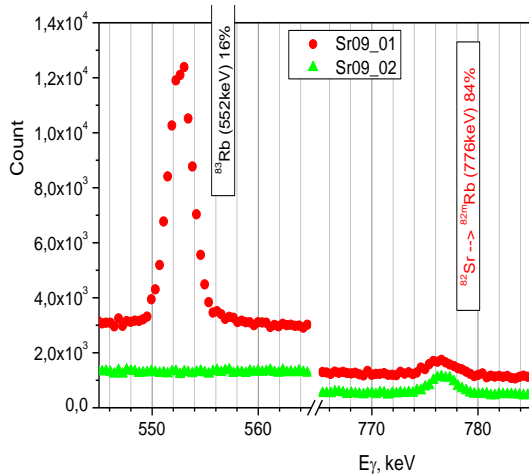
Fig. 3. *On the left* – the spectrum of the vessel with the irradiated RbCl after its heating at a temperature 500 °C (*red dots*) and the spectrum after one hour vessel heating at a temperature 900 °C (*green gots*). *On the right* – the vessel after one hour heating at a temperature 900 °C [5]. It is seen that practically all RbCl powder was evaporate

Therefore, as one can see in Figs. 2 and 3, the separation of strontium isotopes can be performed in a few stages of evaporation of the target material and the produced species by heating the target in a high vacuum at different temperatures. To separate strontium from the rubidium chloride target, the target heating was started at a low temperature 500–900 °C to evaporate the target material RbCl which is considerably higher volatile than strontium atoms. After that, strontium was selectively extracted by washing of internal vessel volume with the HCl solution. Another way of extraction of strontium was to use the niobium or tantalum vessel, which was heated up to 1 700 °C after the target material was evaporated at 900 °C. The evaporated strontium atoms were directed to the collector cooled by floating water. The carried out experiments have demonstrated the efficiency of the target material separation higher than 99.9 %. The efficiency of the strontium radionuclide extraction was about 95 %.

411

4. Experiment description and results of [67]Cu and other radionuclide extraction from irradiated target materials

In the experimental tests for production of [67]Cu, natural metallic Zn was used as a target material. The radionuclide [67]Cu with a half-live 2.57 days is considered as a very perspective radioisotope for therapy of some kinds of malignant tumours. For separation of the target material and the produced [67]Cu radionuclide, the new so called "dry" high temperature method, similar to the one of strontium isotope extraction was utilized. After irradiation by the 1-GeV proton beam at the PNPI synchrocyclotron, metallic zinc was placed into a vessel manufactured from tantalum, which was put into a Ta–W oven heated by direct current. In a high vacuum, the irradiated zinc was heated slowly up to the temperature 700 °C to be evaporated into a separate volume specially constructed to minimize losses of the irradiated material in the process of its evaporation. The process of complete evaporation of the target material of one gram mass (at the temperature of 700 °C) took about one hour. To control the evaporation process, the γ spectrum of the vessel with the irradiated zinc was measured before and after the heating process. Additionally, the vessel after its heating was weighed to control the mass of the evaporated material. In Figures 4a and 4b, a part of the γ spectra of the irradiated sample of zinc is presented [6]. The γ line of the energy 1 115 keV belongs to the decay of [65]Zn with a half-life 244.3 days, and its disappearance indicates the efficiency of the target material evaporation. The fact of complete evaporation of the irradiated zinc target material was confirmed by weighing the sample before and after its heating at 700 °C. The γ line of the energy185 keV belongs to the decay of [67]Cu ($T_{1/2}$ = 2.57 days), which is the produced required radioisotope. The spectrum of the vessel with the irradiated Zn before heating is shown in Fig. 4a by *blue dots*. The spectrum after one hour vessel heating at a temperature 700 °C is shown by *red dots*.

a)   b)
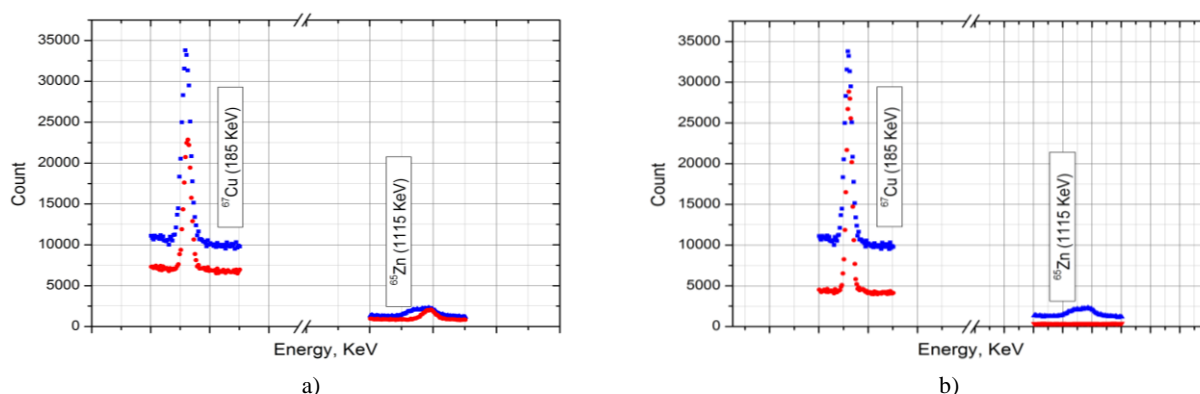
Fig. 4. The spectrum of the vessel with the irradiated Zn before heating is shown by *blue dots*; the spectrum after one hour vessel heating at a temperature 700 °C is shown by *red dots* (a). The spectrum of the evaporated copper atoms collected at the cold finger cooled by floating water after the vessel heating at a temperature 1 460 °C for two hours is shown by *red dots*; for comparison, the spectrum of the vessel with the irradiated Zn before heating is shown by *blue dots* (b)

As one can see, after heating the target material was completely evaporated. It was confirmed by weighing the vessel before and after heating as well. At the same time, the radioactive atoms of copper, having considerably higher boiling point (2 562 °C), remained in the vessel. Also, the presence of the γ line of the energy 1 120 keV of [46]Sc ($T_{1/2}$ = 83.8 days) at the spectrum measured after the target material evaporation (Fig. 4a) demonstrates that atoms of scandium which is a rather hard volatile element (boiling point at 2 830 °C) do not evaporate from the target vessel at a temperature of 700 °C. The spectrum of the evaporated copper atoms collected at the cold finger cooled by floating water after heating the vessel at a temperature 1 460 °C for two hours is shown in Fig. 4b by *red dots*. For comparison, the spectrum of the vessel with the irradiated Zn before heating is also shown (*blue dots*). Therefore, as one can see in Figs. 4a and 4b, for separation of the copper radionuclides and the zinc target material, there should be two stages: the first one is slow evaporation of the target material at a temperature about 700 °C; and the second one is evaporation of the produced copper species by heating the target at a temperature 1 460 °C. The first

experiments carried out demonstrated the efficiency of the target material separation better than 99%. The efficiency of the copper radionuclide extraction and collection was about 90%.

In Figure 5, a slightly different part of the γ spectrum of the irradiated sample of zinc is presented. The γ lines of the energy 1 115 and 1 120 keV belong as in the previous spectra to the decay of ^{65}Zn and ^{46}Sc, whereas the γ lines of the energy 1 039 and 1 099 keV are from the decay of ^{66}Cu, which is a daughter isotope of ^{66}Ni, and from the decay of ^{59}Fe. The irradiated Zn spectrum is shown before heating (*blue dots*) and after two hours heating at a temperature 700 °C (*red dots*). As one can see in Fig. 6, the target material (zinc) was fully evaporated from the heated vessel. The fact of complete evaporation of the irradiated zinc target material was confirmed by weighing the sample before and after its heating. At the same time, the radioactive atoms of Ni, Fe, and Sc, having considerably higher boiling points than the target material (Ni – 2 562 °C, Fe – 2 861 °C, Sc – 2 830 °C), remained in the vessel. The boiling point of the target material Zn is 907 °C. These measurements demonstrate that separation of the target material and the produced radioisotope may be very efficient, if the target material and the produced species have considerably different boiling points. This method of separation of the target material, when the required nuclides do not escape from the target vessel can be used only for production of relatively long-lived radionuclides, as the process of evaporation of the target material may take some hours.
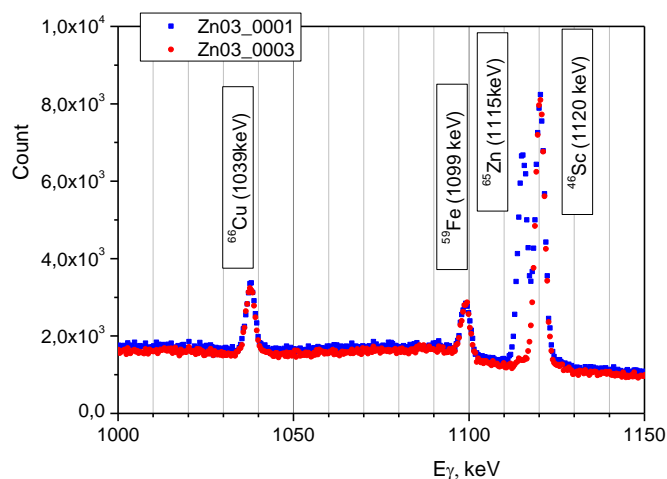
Fig. 5. The irradiated Zn spectrum before heating (*blue dots*) and after two hours heating at a temperature 700 °C (*red dots*)
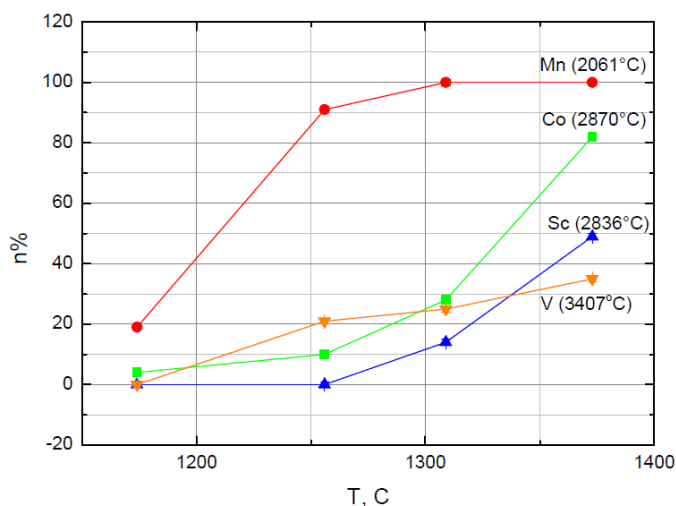
Fig. 6. The evaporated fractions of different radionuclides produced by nuclear reactions in the copper target material and evaporated from it at different temperatures [6]. In the right side in brackets, the boiling points of the evaporated species are presented

413

Similar experiments were carried out with copper as irradiated target material [6]. A metallic copper sample of natural abundance was heated slowly in the tantalum capsule up to the temperature of 1 500 °C. The mass of the evaporated target material was controlled by weighing the sample after each step of its heating. The evaporated amount of the radioactive species was controlled by measurements of their γ-lines integral counts after each step of heating at the defined temperature. In Figure 6, the fractions of atoms of different radioactive isotopes produced by nuclear reactions in the copper target material and evaporated from it at different temperatures are shown. The evaporated fraction is given by the following equation:

$$n = [(N_1 - N_2)/N_1] \cdot 100\%,$$

where N_1 is the appropriate γ-line integral count before heating; N_2 is the same γ-line integral count after heating at the defined temperature.

As one can see in Fig. 6, the evaporated fraction of the radionuclides produced in the measured temperature interval is in good correlation with their boiling point. This makes it possible to rather effectively separate the radionuclides having considerably different boiling points, for example, to separate the radionuclide Mn from Sc or from V.

5. Conclusion

At PNPI, a high current cyclotron C-80 with the energy of extracted proton beam of 40–80 MeV and the current up to 200 μA has been put into operation lately. One of the main goals of C-80 is production of a large number of medical radio nuclides for diagnostics and therapy. At the present time, the construction of the radioisotope complex RIC-80 at the beam of C-80 is carried out. A peculiarity of the proposed radioisotope facility is the use of the mass-separator with the target-ion source device as one of three target stations for on-line and semi on-line production of a high purity separated radio isotopes. An important part of the work was devoted to the developments of targets for the new project RIC-80. The tested target materials will be used to manufacture real target prototypes for the RIC-80 radioisotope complex. The R@D of new high temperature methods of separation of the produced radionuclides ^{82}Sr and ^{67}Cu from the rubidium and zinc irradiated targets was carried out. As it was demonstrated, the new developed high temperature method can be expanded for production of other medical radionuclides. The following stage of the work will be construction of the target unit prototype with the amount of the target material of 40–60 g, which is required for effective medical radionuclide production at the RIC-80.

References

1. V.N. Panteleev *et al.*, *PNPI. High Energy Physics Division. Main Scientific Activities 2007–2012*, Gatchina, 2013, p. 278, http://hepd.pnpi.spb.ru/hepd/articles/PNPI_2007-2012.pdf
2. V.N. Panteleev *et al.*, Rev. Sci. Instrum. **86**, 123510 (2015).
3. S.A. Artamonov *et a*l., *PNPI. High Energy Physics Division. Main Scientific Activities 2007–2012*, Gatchina, 2013, p. 332, http://hepd.pnpi.spb.ru/hepd/articles/PNPI_2007-2012.pdf
4. V.N. Panteleev, Russ. Patent for Invention No. 2598089, The Production Method of Radionuclide Strontium-82, 30 Aug., 2016.
5. V.N. Panteleev *et al.*, Rad. Applic. **1**, No. 2, 95 (2016).
6. V.N. Panteleev, A.E. Barzakh, L.Kh. Batist *et al.*, RAD Conf. Proc. **2**, 43 (2017).

ULTRACOLD NEUTRON DETECTOR

A.G. Krivshich, V.A. Andreev, A.V. Vasiljev, E.A. Ivanov, D.S. Ilyin, A.P. Serebrov

1. Introduction

The problem of the neutron lifetime refinement is related with such important issues of particle physics and cosmology as verification of the Standard Model and the model of nucleosynthesis in the early stages of formation of our universe. By present, the highest accuracy of the neutron lifetime measurements has been achieved by the PNPI group [1, 2]: $t_n = 878.5 \pm 0.8$ s.

The aim of a new experiment is to still further improve the measurement accuracy to the level of 0.2 s. A new spectrometer has been developed to achieve this goal. It is based on the method of ultracold neutron (UCN) storage in a large gravitational trap (UCN source – PF2/MAM) at the Institute Laue–Langevin (ILL, Grenoble, France) [1].

The main spectrometer components were optimized: the volume of the trap was increased by more than a factor of 5, neutron losses on the walls of the trap were reduced due to a new hydrogen-free coatings, the working temperature was lowered down to 80–100 K, and the vacuum was improved to the level of 10^{-7} mbar.

An important part of the spectrometer is the UCN detector which was designed by the Track Detector Department HEPD (PNPI) in collaboration with the Neutron Physics Laboratory of the Neutron Research Division (PNPI).

2. Detector system

The UCN detector is the key unit of the spectrometer, whose working stability determines the accuracy of neutron counting during experimental runs and consequently determines also the accuracy of the neutron lifetime measurement. On this basis, the detector should meet the following requirements:

1. A high UCN detection efficiency, which requires a correct choice of the composition of the working gas mixture in order to reduce primary ionization charge losses in the detector gas volume in the vicinity of the cathode, as well as minimization of neutron losses in the entrance window.

2. Low noise level and low sensitivity to the background.

3. Reliability and long-term neutron counting stability, which is achieved by reduction of the gas leakage and by long-term maintenance of the working gas purity through proper selection of the materials used for the detector construction.

2.1. Detector construction

The design of the gas-filled detector is based on six independent proportional counters (cells), which are placed in a single gas volume. This guarantees that the gas mixture properties are identical in each proportional counter. This constructional concept has already proven itself well in previous experiments.

All counters have the cross-section of 48×46 mm^2 (height $\times$ width), the Au–W anode wire diameter is 25 μm. The lengths of the counters are optimized to cover the maximum detection area (Fig. 1). The respective counter lengths are 165 mm (1 and 6), 252 mm (2 and 5), and 287 mm (3 and 4). These counters are combined in two independent counting channels according to the scheme: 1, 3, 5 and 2, 4, 6.

The entrance window of 290 mm in diameter is made of a thin 100 μm aluminum foil in order to minimize UCN losses. The force acting on the foil at the working conditions is about 6.5 kN. Therefore, a special stainless steel grid is placed in front of the foil to support it from the neutron guide side (vacuum). The optimal pressure of the gas mixture is 1 bar (abs.).

Fig. 1. UCN detector parts: 1 – the upper part of the detector with the entrance window (the grid supporting the entrance foil is seen); 2 – the bottom part of the detector with six proportional counters; 3 – assembled UCN detector, shown from its back side (two preamplifiers and a gas manometer are seen)

2.2. Optimization of the electric field structure

The structure of the electric field within each of the proportional counters was optimized in order to minimize a negative impact of the detector design on the measured amplitude spectra.

1. Compared to the previous prototype, the design of the detector was changed to remove the drift space with non-uniform electric field that is located near the entrance window (Fig. 2).

2. The construction of the cathodes was optimized to provide a symmetrical structure of the electric field in the transverse direction of each anode wire.
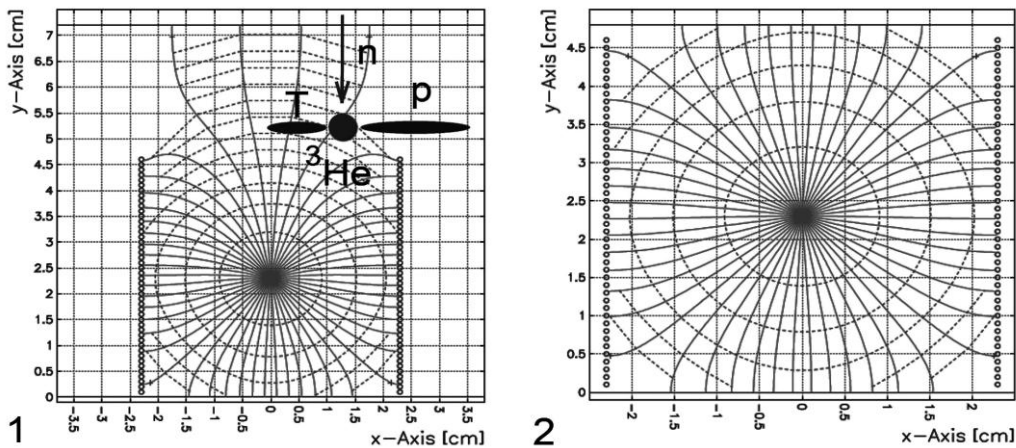
Fig. 2. The structure of the electric field and the timing diagrams in a cell calculated with GARFIELD [3] for a gas mixture 30 mbar ^{3}He + 970 mbar CF_4 and an anode voltage of 2 kV: 1 – prototype cell; 2 – improved cell. The *solid lines* are the drift lines of electrons; the *dotted lines* are the electron time contours in time steps of 0.1 μs

The measures taken greatly improved the detector characteristics:

1) a high uniformity of the gas gain along the anode wires was achieved and the maximal fluctuations did not exceed ±4%;

2) cross-talks between neighboring cells (counters) caused by ingress of parts of the proton–tritium tracks that trigger two independent events with smaller amplitudes were practically excluded (Fig. 2);

3) the maximum time required to collect the ions formed in a gas avalanche was reduced by more than a factor 8, thus not exceeding 10^4 μs.

2.3. Principle of ultracold neutron registration

The neutrons are detected through the nuclear reaction $^3He + n \rightarrow p + T + 764$ keV. Since the reaction cross-section is inversely proportional to the neutron velocity v, one obtains $\sigma_{UCN} = \sigma(1.8\ \text{Å})\,v(1.8\ \text{Å})/v_{UCN}$, where $\sigma(1.8\ \text{Å}) = 5\,333$ b; $v(1.8\ \text{Å}) = 2\,200$ m/s; $v_{UCN} = 8$ m/s; $\sigma_{UCN} \approx 1.5 \cdot 10^6$ b.

In accordance with the momentum conservation law, the particles acquire kinetic energies $E(p) = 573$ keV and $E(T) = 191$ keV, respectively. They are emitted in opposite directions from the point of interaction and produce primary ionization charges. The centre of gravity (c. g.) of this charge cloud is shifted relative to the interaction point by a distance $R_{sph} = 0.35R(p)$, where $R(p)$ is the proton range. So, the c. g. of charges are placed on a spheroid surface of radius R_{sph} for all neutrons absorbed at the same point.

2.4. Detector efficiency and the "wall" effect

The key factor in achieving an effective rejection of the background from the "neutron" events is to minimize the "wall" effect [4], which is associated with a partial loss of the primary ionization charge near the cathode walls. The largest contribution comes from the tracks which are formed near the entrance window (Fig. 3).
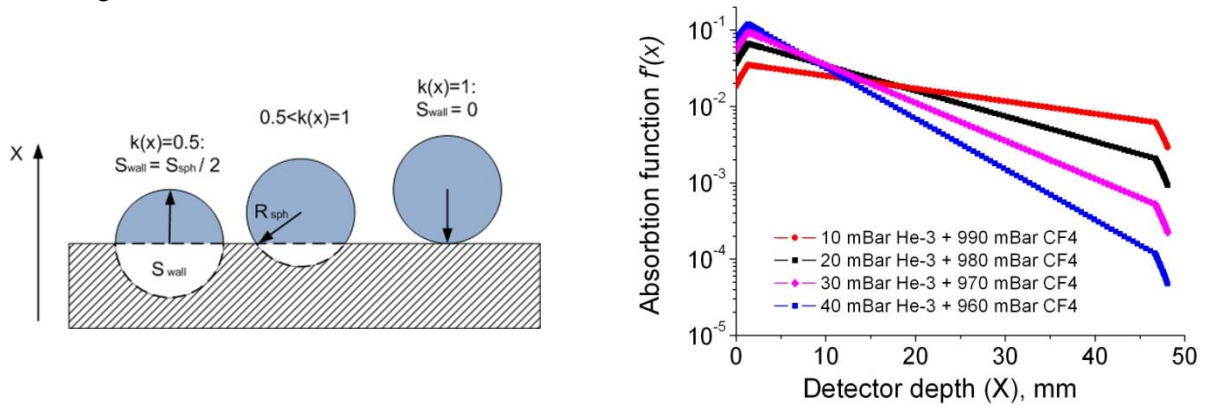
Fig. 3. The influence of the "wall" effect: the illustration for explaining the calculation of the correction factor $k(x)$ (*left*); the function $f'(x)$ for various compositions of the gas mixture (*right*)

The degree of influence of the "wall" effect is determined by two main factors: 1) the probability function $f(x)$ of the UCN absorption which depends on the partial pressure of ^3He; 2) the ranges of protons and tritons in the gas mixture, which are determined by the partial pressure of the stop-gas CF_4 or Ar.

The ranges of the particles were calculated with the SRIM program [5]. The results for Ar and CF_4 are $R_{sph}(CF_4) \approx 1.5/P$ [mm/bar] and $R_{sph}(Ar) \approx 3.8/P$ [mm/bar], where P is the absolute gas pressure in bar.

The UCN absorption efficiency $\varepsilon(L)$ and the probability function of absorption $f'(x)$ are:

$$\varepsilon(L) = \int_0^L f'(x)dx,$$

$$f'(x) = f(x)k(x),\ f(x) = n\sigma e^{-n\sigma x},\ k(x) = 1 - S_{wall}/S_{sph},$$

where $L = 48$ mm is the detector thickness; n is the concentration of ^3He; σ is the cross-section for the reaction $^3He(n, p)T$, and $k(x)$ is a correction factor accounting for the "wall" effect (front and back walls of the cell in the x direction). S_{wall} is the area of the circle segment with $r = R_{sph}$ truncated by the cathode wall, S_{sph} is the area of the full circle, and x is the coordinate along the beam direction (from the window to the back), as indicated in Fig. 3.

The correction factor $k(x)$ varies from 0.5 to 1. So, there are a few cases: 1) $k = 1$ for complete p–T tracks, 2) $0.5 < k < 1$ for truncated tracks, 3) $k = 0.5$ when the absorption point of the neutron (the centre of the spheroid) coincides with the wall surface. Events with $k < 0.5$ are not taken into account.

The "wall" effect value W of the cell takes into account all walls: $W = (1 - S/S_0)$, where

$$S_0 = \int_{X_{min}}^{X_{max}} \int_{Y_{min}}^{Y_{max}} f(x)dxdy$$

is the "effective" area of the cell ($X_{min} = Y_{min} = 0$ mm, $X_{max} = 48$ mm, $Y_{max} = 46$ mm) and

$$S_0 = \int_{X_{min}}^{X_{max}} \int_{Y_{min}}^{Y_{max}} f'(x)k(x)dxdy$$

is the "effective" area of the cell including wall effect corrections (front, back, and side walls of the cell), and $k(y)$ is the correction factor in the direction perpendicular to the x-axis and accounts for the side walls of the cell. The results of the calculations are shown in Fig. 4.
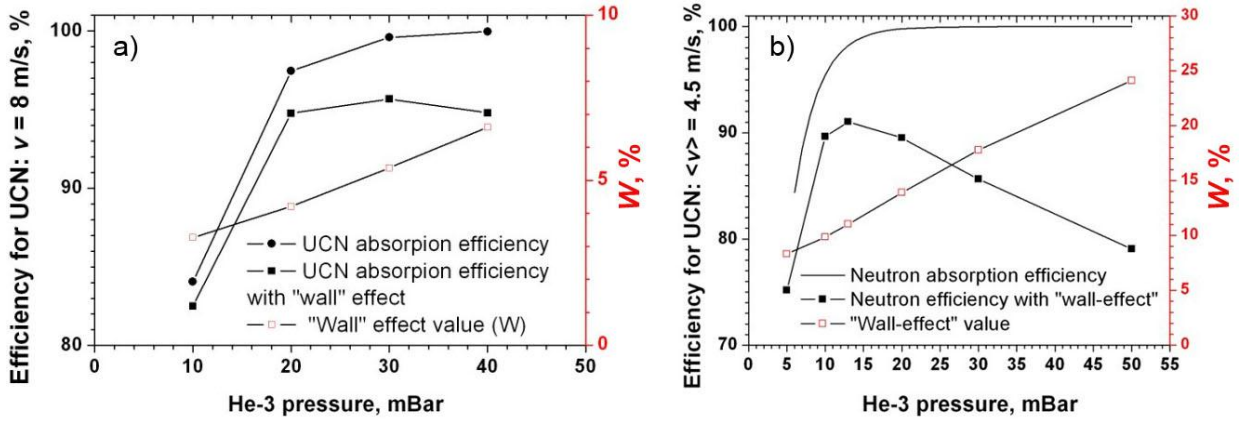
Fig. 4. Calculated efficiency and the "wall" effect value W versus the partial pressure of ^{3}He in the gas mixture: a – for the UCN velocity $v = 8$ m/s and the gas mixture ^{3}He–CF$_4$; b – for the average UCN velocity $v = 4.5$ m/s in the UCN spectrometer at the ILL and the gas mixture ^{3}He–Ar–CO$_2$. W is the fraction of truncated tracks in %

2.5. Choice of the gas mixture

The gas mixtures were carefully selected to minimize the "wall" effect and to achieve the maximal UCN efficiency.

For the initially planned UCN velocity $v = 8$ m/s, we choose the gas mixture ^{3}He–CF$_4$ which is conventional for thermal neutron detectors. For this gas mixture, the optimal pressure of ^{3}He is 30 mbar (see Fig. 4a). The maximal efficiency $\varepsilon_{UCN} \approx 95\%$ and a small "wall" effect value $W \approx 5.5\%$ were achieved for that ^{3}He pressure. The partial pressure of CF$_4$ was 1 030 mbar, limited by the maximum operational pressure (see Section 3.1).

The final composition of the gas mixture was optimized during detector tests under real experimental conditions. The real mean UCN velocity was $\langle v \rangle = 4.5 \pm 1.0$ m/s. For this case, the initial choice of the ^{3}He pressure 30 mbar was not optimal (see Fig. 4b), since the "wall" effect value $W \approx 17\%$ was high and the UCN efficiency $\varepsilon_{UCN} \approx 85\%$ was relatively low.

Therefore, the ^{3}He pressure was reduced to 13 mbar to achieve the maximal efficiency $\varepsilon_{UCN} \approx 91\%$ and to minimize the value of W down to $W \approx 11\%$. To reduce the operating voltage and consequently the high-voltage noise, the finally selected working gas mixture was 13 mbar ^{3}He + 1 060 mbar Ar + 20 mbar CO$_2$.

3. Detector tests

3.1. Lab tests (PNPI, Russia)

The detector was successfully tested both at the PNPI lab with a Pu–Be source and as a part of the UCN spectrometer at the PF2/MAM beam port of the ILL high-flux reactor in Grenoble. In particular, the gas gain non-uniformity along the anode wire was confined to be ±4 % for all cells, and the amplitude spectra were the same for both channels. An amplitude resolution $\Delta E/E$ = 6–15% (full width at half maximum) was obtained in the operating range of the anode high voltage HV = 1.7–1.9 kV.

3.2. Reactor tests (ILL, France)

The detector was installed at the UCN spectrometer at the HFR reactor in Grenoble. As mentioned before, the mean UCN velocity at the PF2/MAM beam port was v = 4.5 ± 1.0 m/s. The initial measurements with a ^{3}He–CF$_4$ gas mixture showed a significant number of "neutron" events with incomplete ionization tracks – low-amplitude tails in the amplitude spectra (Fig. 5a).

The impact of low-amplitude events on the amplitude spectra was significantly reduced by optimization of the gas mixture composition, as can be clearly seen in Fig. 5b from the counting rate reduction at the tritium energy level.
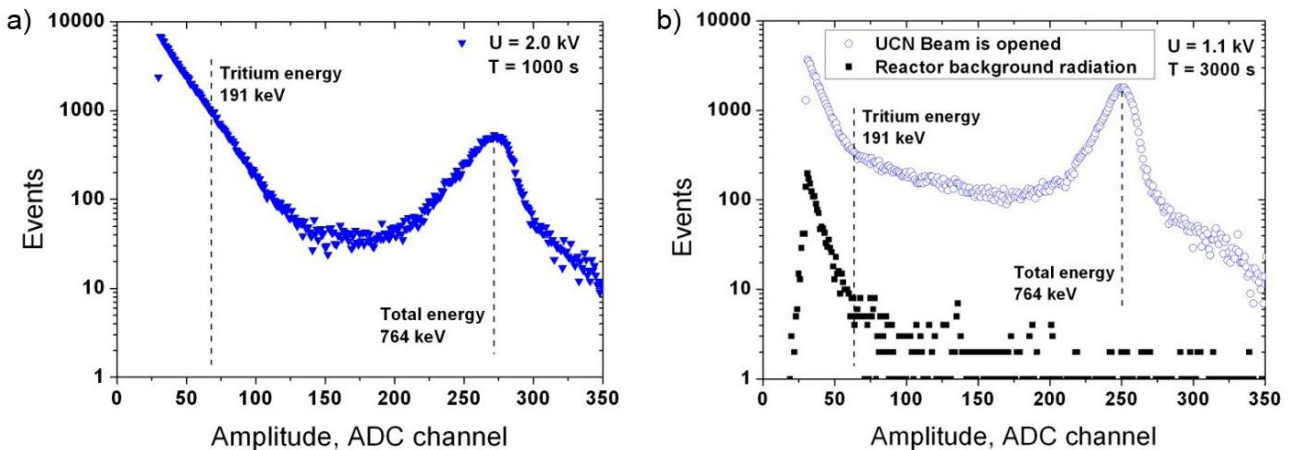
Fig. 5. Amplitude spectra obtained with the second counting channel of the detector at the UCN spectrometer at the HFR reactor with the thermal power 30 MW: a – for the ^{3}He–CF$_4$ gas mixture (UCN irradiation); b – for the working gas mixture ^{3}He–Ar–CO$_2$ (UCN and reactor background irradiation). Tritium and total reaction energy levels are indicated by *dotted lines*

Indeed, the gas mixture optimization improved the shape of the amplitude spectra, allowing for a more effective background rejection because a smaller number of "neutron" events were lost after amplitude discrimination.

4. Conclusion

The UCN detector has been designed and successfully tested. Currently it is used at the UCN spectrometer at the ILL Grenoble.

It has been shown that the influence of the "wall" effect on the structure of the UCN amplitude spectrum manifests itself in an additional continuous spectrum from background up to the total energy peak E_0 = 764 keV.

The negative impact of this effect offers a difficulty in rejecting background events from "neutron" events, since a significant number of such events have incomplete ionization tracks and, as a result, have low amplitudes.

References

1. A. Serebrov *et al.*, J. Tech. Phys. **83**, No. 11, 136 (2013).
2. A. Serebrov *et al.*, Phys. Rev. C **78**, 035505 (2008).
3. R. Veenhof, Garfield – Simulation of Gaseous Detectors, http://consult.cern.ch/writeup/garfield
4. R. Batchelor *et al.*, Rev. Sci. Instrum. **26**, 1037 (1955).
5. J. Ziegler, Srim – the Stopping and Range of Ions in Matter, http://www.srim.org/

UNIVERSITY OF FLORIDA–PNPI HIGH VOLTAGE SYSTEM IN THE CMS ENDCAP MUON DETECTOR

S.S. Volkov, S.V. Bondarev, V.L. Golovtsov, N.B. Isaev, E.M. Orischin, L.O. Sergeev, L.N. Uvarov

The design and construction of the University of Florida (UF) – PNPI high voltage system (HVS) was performed in collaboration with specialists of the UF [1] for three detecting stations ME1/2, ME1/3, ME2, ME3, and ME4 of each of the two endcaps in the CMS endcap muon system (EMU) [2]. In total, there are 234 cathode strip chambers (CSC) per each endcap as it is shown in Fig. 1. The detecting stations are divided into two regions each: ME1/2 and ME1/3, ME2, 3, 4/1 and ME2, 3, 4/2. At present, there are 468 six-plane CSC. Each plane should be provided with a high voltage (HV) line. Moreover, the HV line in each layer is subdivided into several segments (Fig. 2). Five segments are in the chambers ME2/2, ME3/2, ME4/2, and 3 segments are in all other chambers.
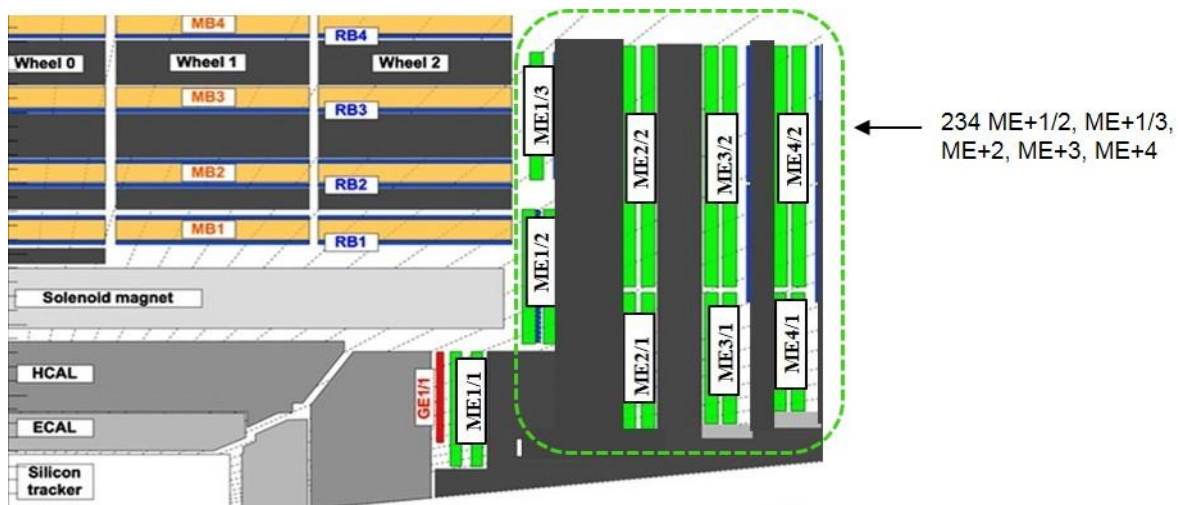
Fig. 1. Structure of the CMS endcap muon system
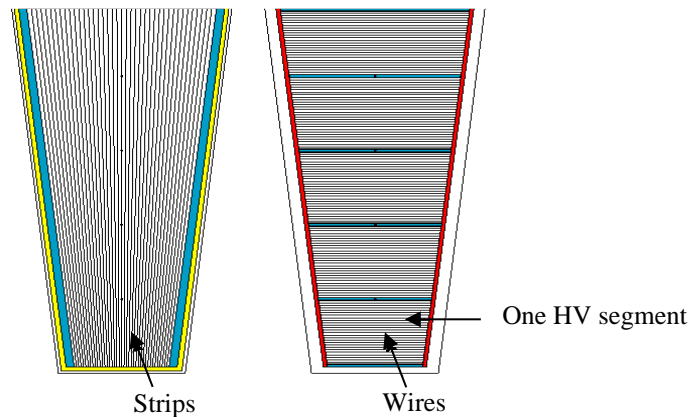
Fig. 2. Structure of the CSC with five HV segments

The main purpose of the HVS is to provide high voltage for the CMS endcap CSCs. CSC features that affect the HVS design are the following:
- small HV segments and high tolerance to HV failures,
- the same working voltage with small variation from segment to segment,
- a problematic segment can be fixed by reducing voltage or disconnecting from HV,

421

- precise consumption current for each segment,
- detects discharges and leaks.

Figure 3 shows the overall hierarchical structure of the HV distribution in the HVS.
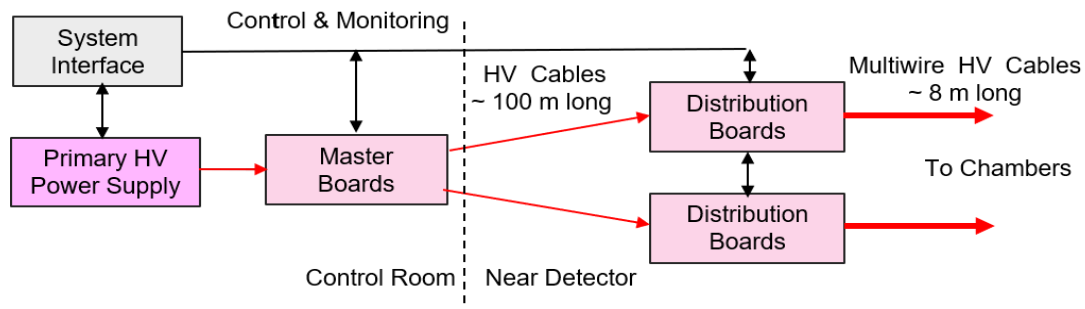
Fig. 3. HVS distribution structure

The custom-made HVS has a three-tier structure. There are eight commercial Matsusada primary HV power supplies (PHVPS). They provide the HV power to 50 master boards, each of which has eight regulated outputs. Both the PHVPS and the crates with the master boards are located in underground service cavern (USC). The master board outputs are routed to the distribution boards located near CSCs (on the periphery of the endcap discs). There are two types of distribution boards: 216 30-channel boards serve ME2/2, ME3/2, ME4/2 chambers (one chamber per board); 126 36-channel boards serve ME2/1, ME3/1, ME4/1, ME1/2, ME1/3 chambers (two chambers per board). The system interface consists of a control computer and control boards, which provide control and monitoring operation for each channel of the HVS. Table 1 summarizes the quantities of different hardware components in the HVS.

Table 1

Summary of hardware components in the HVS

Component	Quantity
Primary high voltage power supply	8
Control computers	2
Low voltage power supplies	2
Control boards	4
Master boards	50
Distribution boards, 30 channels	216
Distribution boards, 36 channels	126
Independently regulated and monitored distribution channels	11 016

There are eight PHVPSs in the system. All of them are located in the control room. Each of these modules supplies high voltage to one of eight partitions of the HVS. PHVPS is a commercially available module, manufactured by Matsusada Precision with the following parameters:
- AU-5P60-LF(U) HV power supply, 5 000 V / 60 mA;
- GP-HV-L(U) control interface;
- RS-232C module for control interface.

The master boards are located in the control room, and they receive HV generated by PHVPS and distribute it to its eight outputs. Each output is independent and capable of
- regulate voltage from 0 to 4 000 V,
- deliver up to 1.5 mA of current into the load,
- voltage measurement from 0 to 4 000 V,
- current measurement from 0 to 1.5 mA,
- over-voltage and over-current protection with programmable threshold.

The distribution boards are located in underground experimental cavern (UXC), in racks near the discs, to minimize the length of the cables that deliver voltage from them to all chambers. Each distributor board receives high voltage from the master board *via* very long cable and distributes it to its 30 or 36 outputs. Each output of a distribution board is independent and capable of

- regulate voltage up to 1 000 V down from maximum voltage supplied from the master board output,
- deliver up to 100 mkA of current into the load,
- voltage measurement from 0 to 4 000 V,
- current measurement from 0 to 100 mkA,
- over-voltage and over-current protection with programmable thresholds and timeouts.

Each distribution board output provides power for one HV segment of a CSC.

Two computers control the entire HVS. Both computers are located in USC. Figure 4 shows the software structure and control interfaces of the HVS. The software was designed and maintained by specialists of the UF.
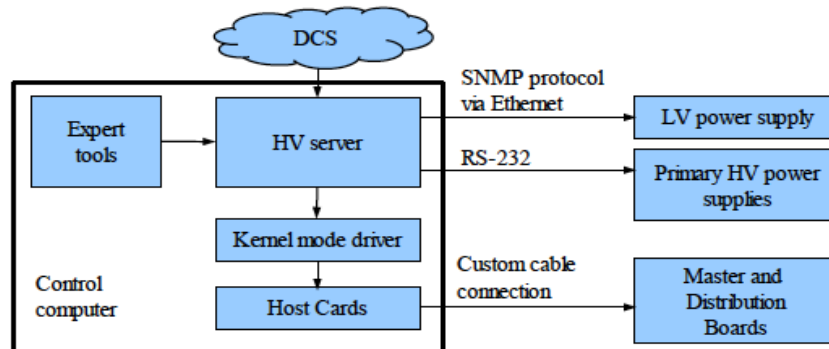
Fig. 4. Software structure and control interfaces of the HVS

The HV server is based on the distributed information management (DIM) system [3] and performs the following tasks:

- receives high-level commands from detector control system graphical user interface or from expert tools;
- decodes these commands; passes the corresponding parameters to the kernel mode driver, the PHVPS and the low voltage power supply (LVPS);
- reads out and publishes the monitoring information from all master and distribution boards, the PHVPS and the LVPS.

The main purpose of the kernel mode driver is to provide control and monitoring of the master and distribution boards in real time:

- over-current and over-voltage trips,
- voltage ramp-up and ramp-down,
- pre- and post-trip data logging for future analysis.

There are several standalone expert tools that can be run on the HVS control computer. They provide control of one or multiple components of the system including:

- displaying voltages, currents, voltage and current trip levels and timeouts, states of all channels of the selected component;
- setting any of the above parameters using simple command-line interface;
- each channel calibration for voltage setting, voltage, and current sensors;
- trip profile analysing in case of overcurrent or overvoltage.

As a result, the HVS has a developed hardware and software basis to provide stable operation for a number of years. Table 2 shows the number of channel and board failures by years. Elevated failures in 2009 are due to the replacement operation of the batch of resistors with unstable parameters. Elevated failures in 2014 are due to the system upgrade with new boards installation for ME4/2.

Table 2

HVS channel and board failures

Year	Distribution board – 36		Distribution board – 30		Master board	
	Single channel	Board	Single channel	Board	Single channel	Board
2009	23	1	30	2	3	1
2010	11	1	4	0	0	0
2011	4	16	6	1	1	1
2012	4	1	2	1	0	0
2013	0	0	0	0	0	0
2014	0	1	6	6	2	1
2015	2	0	0	0	2	1

Figure 5 shows the voltage calibration stability in time during one year. The drift is negligible. The voltage calibrations are now tested periodically for all channels.
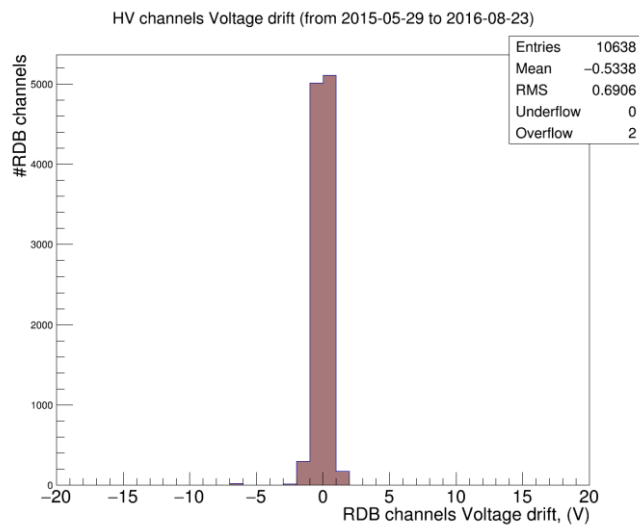
Fig. 5. HVS high voltage channels drift in time

References

1. A.A. Vorobyov *et al.*, *PNPI. High Energy Physics Division. Main Scientific Activities 2002–2006*, Gatchina, 2007, pp. 26–34.
2. A.A. Vorobyov *et al.*, *PNPI. High Energy Physics Division. Main Scientific Activities 2007–2012*, Gatchina, 2013, p. 27.
3. DCS Users Manual, https://twiki.cern.ch/twiki/bin/view/CMS/CSCOperationsDCS

NONINVASIVE METHOD OF RECOVERY OF GAS PARTICLE DETECTORS UNDER OPERATION IN HIGH-INTENSITY FIELDS OF RADIATION

V.A. Andreev, G.E. Gavrilov, A.G. Krivshich, D.A. Maisuzenko, A.A. Fetisov, N.Yu. Shvetsova

1. Introduction

Here we describe a method of noninvasive recovery of gas-discharge detectors, which have been degraded due to operation in intense radiation fields. The proposed techniques are based on the plasma-chemical reactions, which occur during the detector training in the gas discharge that is generated in a special gas mixture. It has been shown that the method of plasma-chemical etching in a gas discharge increases the detector lifetime in several times.

Usually, aging effects result in a surface degradation of both the anode and cathode electrodes, which occur in different forms. The first one is the anode type of aging. First of all, it is associated with silicon deposits formed on the surface of the anode wires. The source of these deposits are structural materials and elements of the gas supply system of the detector [1]. These effects are manifested even with small accumulated charges in the range of 0.1–1.0 C/cm of the anode wire length. If there would be no silicon contamination in the detector, it could operate at higher doses with the accumulated charge exceeding 1 C/cm. In that case, the main mechanism of aging would be swelling of the wire caused by chemical interaction of the oxygen which is coming from the gas avalanche with the tungsten which is the main material of the anode wire [2].

The second type of aging is the cathode aging. It is associated with formation of dielectric films at the cathode, which usually cause the Malter effect (ME) [3, 4] – spontaneous self-sustained current in the detector initiated by electron emission from the cathode surface through dielectric films formed at the cathode.

The explanations of these mechanisms can be considered in terms of plasma chemistry. Different types of chemical radicals and ions are produced in the gas avalanche near the anode wire. They can cause plasma chemical reactions. Polymers and other chemical compounds resulting from these reactions may deposit on the surface of the detector electrodes and due to interaction with the electrode materials may form even new chemically different substances.

A noninvasive method of cleaning the cathode and anode wire surface from organic compounds, silicon, and tungsten compositions (swelling effects) has been developed at PNPI. It is based on the plasma-chemical etching reactions which are used in the microelectronics production. Recovery of the main technical characteristics of the detector after its aging without disassembling and repairing is actual for many physical experiments, since the development of a detector operating with an accumulated charge of about 10–20 C/cm is still a problem.

2. Malter effect at the cathode

For recovery of multiwire proportional chambers (MWPC) of the muon tracker in the LHCb experiment at the Large Hadron Collider from the ME, the 40% Ar + 55% CO_2 + 5% CF_4 working gas mixture with added 2% of oxygen was tested. The oxygen radicals and ozone produced in the gas discharge plasma near the wire interact efficiently with organic and silicon films at the cathode, forming volatile compounds, which are removed in the process of gas flushing [5, 6]. Figure 1 shows the Malter current as a function of MWPC training time. The ME current on a level of 25 μA was ignited by ^{90}Sr β-source irradiation at a voltage of 2 600–2 700 V and maintained by increasing the voltage step by step up to the maximum value 2 850 V; the ME current decreases as the formations at the cathode are removed. As one can see, during four hours of MWPC training in the gas mixture with 2% oxygen, the ME nearly vanished. In contradictory to this, the current remained virtually constant even after six hours of MWPC training in the working gas mixture. This method was used to recover four MWPC units, which could not be recovered by training in the working gas mixture.
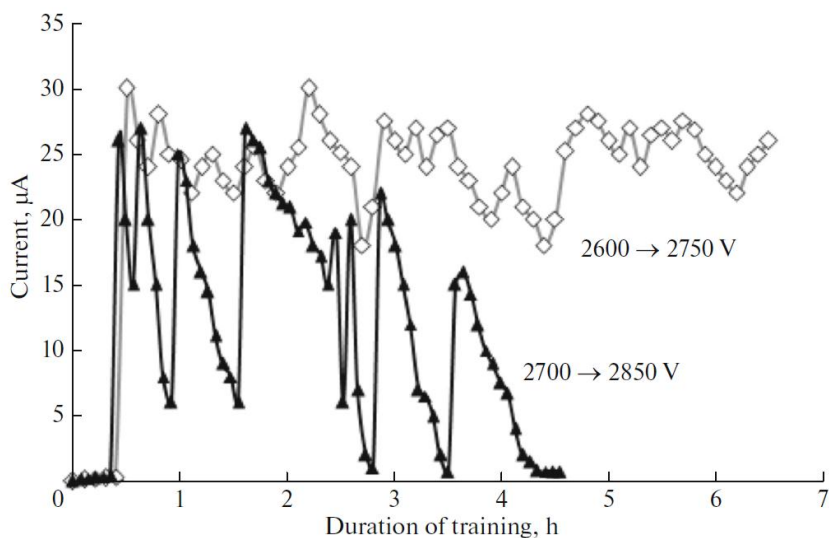
Fig. 1. Malter current in a MWPC during recovery: ◊ – training in the working gas mixture; ▲ – gas mixture with 2% O_2 added

3. Anode wire recovery

The etching of various types of formations on the anode wire surface took place in the gas-discharge plasma that is generated in the 80% CF_4 + 20% CO_2 gas mixture near the anode wire with a negative potential. The basis of the process is the plasma-chemical etching by fluoride active radicals both silicon and tungsten containing compounds in the gas discharge in the vicinity of the anode wire.

In the course of the wire recovery, the damaged region is irradiated by a ^{55}Fe source. *X*-ray photons with an energy of 5.9 keV maintain ionization in the gas-discharge plasma and provide desorption of the etching products [7–9]. The etching efficiency of silicon and tungsten formations was studied with the use of proportional straw counters.

The experimental results of the straw recovery from silicon formations are shown in Fig. 2. The diameter of the anode wire in the straw was 50 μm, the diameter of the cathode-polyamide tube with deposited carbon was 4 mm. The straw aging effects were studied in a gas mixture of 60% Ar + 30% CO_2 + 10% CF_4. This straw was irradiated by a ^{90}Sr β source with a total intensity of about 15 MHz. The anode wire was aged three times in a silicon-contaminated gas mixture until the amplitude was reduced by ~ 35%, and each time the anode wire recovered in the 80% CF_4 + 20% CO_2 gas mixture.

Figure 2a shows the wire surface pictures from the scanning microscope and the *X*-ray fluorescence analysis spectra (SEM/XEM) of the wire surface before and after three "aging–recovery" cycles. As one can see, the wire diameter has increased from 50 to 59 μm (18%). Intensive peaks of silicon and oxygen are observed on the anode wire surface.

Figure 2b shows the gas amplification factor (GAF) behaviour as a function of the accumulated charge. In order to be sure that the recovery effect exists for silicon polluted anode wires, two independent straws were aged and recovered. Each of them was subjected to this procedure three times. The obtained results were very similar (see Figs. 2a and 2b), which confirmed the effectiveness of the proposed method.
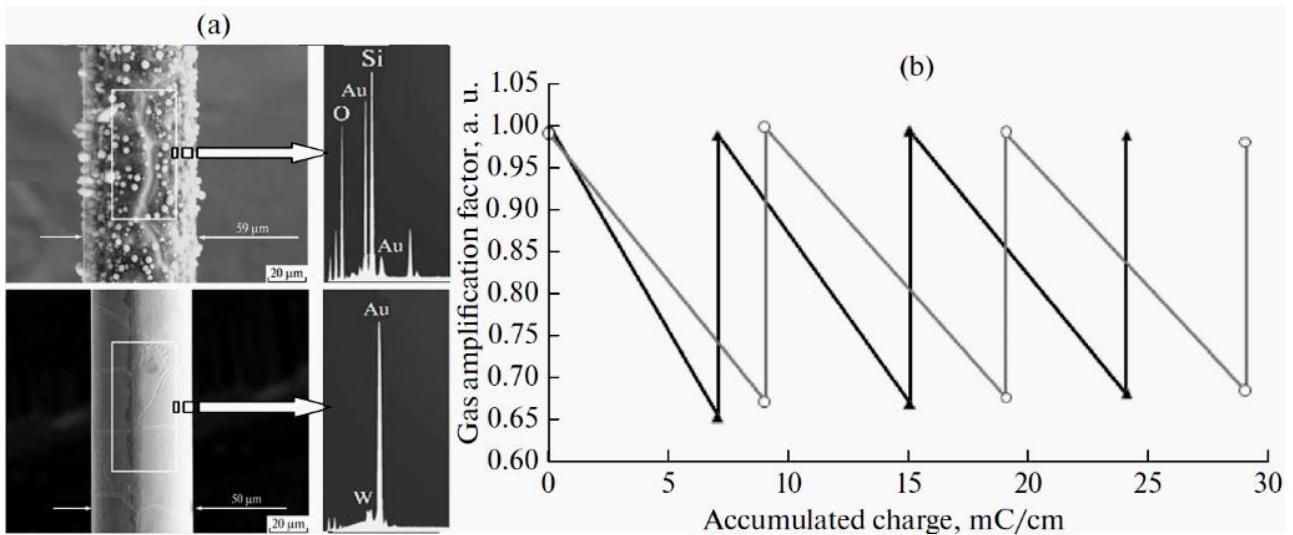
Fig. 2. Results of a SEM/XEM examination of the surface of an aged anode wire (*upper part*) and of a wire recovered by the etching procedure (*lower part*); on the *right side* – results of a XEM spectra analysis of the wire surface are shown (a). GAF as a function of the accumulated charge during multiple recovery of two counters (b): ▲ – straw-1; O – straw-2; *slanting lines* – the GAF reduction during irradiation; *vertical lines* – the GAF recovery during etching

For achieving the anode swelling effect, a clean gas system was used. In order to be sure that the recovery effect exists for swelled anode wires, two independent series of measurements were performed, for each of them the aging-recovery cycles were repeated three times. The obtained results were very similar (Figs. 3a and 3b). In the first series, straws were irradiated until the signal amplitude dropped down by ~ 6%, and in the second series, it dropped down by ~ 3% [10]. The results of measurements are shown in Fig. 3. Figure 3a shows a SEM/XEM analysis of the anode wire surface. A film of tungsten-oxide compound is clearly observed on the gold coating of the wire. Figure 3b shows the GAF behaviour as a function of the accumulated charge.
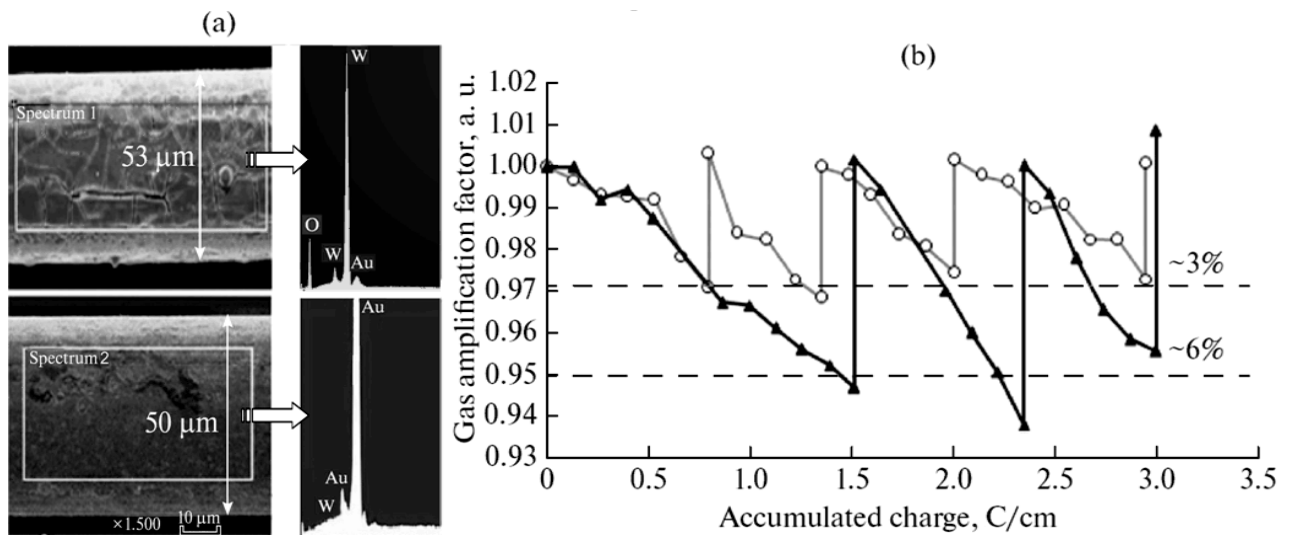
Fig. 3. Results of a SEM/XEM examination of the surface of an aged wire (*upper part*) and of a wire aged and three times cleaned (*lower part*); on the *right side* there are results of a XEM spectra analysis of the wire surface measured in a rectangular area indicated by a white line on the *left side* (a). GAF as a function of the accumulated charge during multiple recovery of counters (b): ▲ – straw-1; ○ – straw-2 [10]

4. Conclusion

Application of the proposed method of the plasma-chemical etching in a gas discharge to recover the aged gas-discharge detectors increases the detector lifetime by several times. This method of recovery has a universal character and can be a suitable solution to the problem of detectors aging in future experiments.

References

1. M. Capeans, Nucl. Instr. Meth. Phys. Res. A **515**, 73 (2003).
2. T. Ferguson, G. Gavrilov, V. Gratchev *et al*., Nucl. Instrum. Meth. Phys. Res. A **515**, 266 (2003).
3. L. Malter, Phys. Rev. **50**, 48 (1936).
4. J. Va'vra, Nucl. Instrum. Meth. Phys. Res. A **515**, 1 (2003).
5. F.I. Grigor'ev, *Plasma-Chemical and Ion-Chemical Etching in Microelectronic Technology, Textbook*, Mosk. Gos. Univ., Elektron. Mat., Moscow, 2003 [in Russian].
6. A.M. Boyarsky, Nucl. Instrum. Meth. Phys. Res. A **604**, 573 (2009).
7. V.P. Zhuze, B.V. Kurchatov, Physik. Z. Sowjetunion **2**, 453 (1932).
8. S. Belostotski, S. Frullani *et al*., Nucl. Instrum. Meth. Phys. Res. A **591**, 353 (2008).
9. G.E. Gavrilov, V.M. Vakhtel, A.G. Krivshich *et al.*, Preprint PNPI-2983, Gatchina (2015).
10. G.E. Gavrilov, D.A. Aksenov, R. Conti *et al.*, Nucl. Instrum. Meth. Phys. Res. A **694**, 167 (2012).

RECOVERY OF GAS DISCHARGE DETECTORS FROM MALTER EFFECT

G.E. Gavrilov, E.V. Kuznetsova, O.E. Maev, D.A. Maysuzenko, S.A. Nasybulin

1. Introduction

Aging or degradation of operating characteristics of gas discharge detectors remains a real problem in modern high energy physics experiments with high radiation background levels. According to results of numerous studies [1, 2], very often aging of gaseous detectors is caused by residual contamination of silicon compounds in the working gas mixture. Silicon is the most widespread element which is regularly registered in analyses of precipitates formed on electrode surfaces. The working gas mixture can be contaminated by a gas circulation pump, gas system connections, and fiberglass electrodes of the detector.

Polymerization reactions take place near the wire in the gas discharge plasma, and the formed polymers precipitate on the surface of anode wires as well as on cathode planes, causing degradation of operation characteristics of the detector. The presence of dielectric polymer films on the conducting metal cathode surface (wires or plane) as a rule results in appearance of a self-sustained secondary emission current, the so-called Malter effect (ME) [3, 4]. This current is the result of accumulation of a positive electric charge on a thin (< 1 μm) film during the operation of the chamber. Depending on the charge value and the thickness of the dielectric film, the resulting electric field may become sufficient to cause spontaneous secondary electron emission-from the cathode.

For gas discharge detectors, the ME is the most devastating of all secondary electron emission effects. It appears when formation of the electric charge is not compensated by a leakage current from the film surface. Multi-wire proportional chambers (MWPC) operating in a high radiation environment may demonstrate a self-sustained current reaching up to 30–50 μA. The ME results in an increased noise rate, in trips of the high-voltage supply system due to high currents exceeding the usual safe limits, and in the accelerated aging of anode wires around the zone of ME occurrence.

A number of MWPCs operated by the LHCb experiment at the Large Hadron Collider (LHC) demonstrate appearance of the ME. In this work, a noninvasive recovery method of quick and efficient ME current suppression is described. This approach was successfully applied to problematic chambers of the LHCb muon detector and brought them back to a nominal operation. Recovery of gas discharge detectors from aging without disassembling and repair is topical for many modern experiments and often is a challenging task.

2. Curing Malter effect in multi-wire proportional chambers in presence of CF$_4$

The ME is well known to experimentalists for many years. In some cases it can be cured by adding up of 0.2% of water vapour or 2–3% of various alcohols to the working gas mixture [2, 5]. Molecules of water and alcohol stop the polymerization processes in the gas mixture and precipitation on the cathode surface, and rapidly increase its conductivity. However, these additives cannot be applied to all types of MWPCs. Water vapours deposited on the surface of electrodes and insulators cause micro-sparks, and alcohol vapours, being solvents, cause deformation and swelling of dielectric elements of the detector construction [5].

Because of the above limitations, neither water nor alcohol vapours were considered for eliminating the ME in MWPCs of the muon detector at the LHCb experiment. At the same time, the presence of CF$_4$ in the working gas mixture of the muon detector (40% Ar + 55% CO$_2$ + 5% CF$_4$) allows one to cure the ME without using potentially dangerous admixtures.

CF$_4$ is often added to MWPC gas mixtures to prevent chamber aging caused by silicon deposits on anode wires [1, 6]. Moreover, CF$_4$ is widely used in microelectronics and microelectromechanical device production for plasma etching of Si, SiO$_2$, and, in presence of oxygen, of various polymer materials [7–11]. Fluorine radicals produced in plasma react with silicon and polymers, resulting in the surface etching by forming volatile products.

In proportional chambers, the most intensive formation of free radicals takes place around anode wires, where the electric field reaches $20-200$ kV $\cdot$ cm^{-1}. Electron impact dissociation of CF_4 molecules at the electron energy of about $E_e \approx 3-5$ eV occurs with formation of the following chemically active radicals [7, 8]:

$$e^- + CF_4 \rightarrow CF_3^+ + F^\bullet + 2e^-, \tag{1}$$
$$e^- + CF_4 \rightarrow {}^\bullet CF_3 + F^\bullet + e^-, \tag{2}$$
$$e^- + CF_4 \rightarrow {}^\bullet CF_2 + 2F^\bullet + e^-. \tag{3}$$

$^\bullet CF_3$, $^\bullet CF_2$, and $F^\bullet$ radicals produced in plasma-chemical reactions (1–3) efficiently react with different silicon formations. Volatile molecules (CO_2, O_2, and SiF_4) formed in etching reactions (4–6) are easily removed from the detector volume with the gas flow:

$$4F^\bullet + Si \rightarrow SiF_4\uparrow; \tag{4}$$
$$4F^\bullet + SiO_2 \rightarrow SiF_4\uparrow + O_2\uparrow; \tag{5}$$
$$Si + {}^\bullet CF_3 + F^\bullet + 2O \rightarrow SiF_4\uparrow + CO_2\uparrow. \tag{6}$$
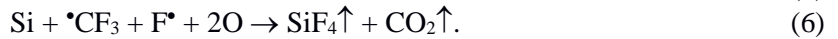
To recover MWPCs from the ME caused by silicon or organic films on the cathode surface, the corresponding depositions should be etched. However, near the cathodes, which are located at a distance of several millimeters from the anode wires, the concentration of fluorine radicals is low. Therefore, the recovery procedure often requires a relatively long time.

3. Recovery procedure developed for the muon detector of the LHCb experiment

The muon detector consists of 1 368 modules of 19 different types covering a total area of 435 m^2. Despite different dimensions, each module has the same internal geometry and consists of four or two MWPC gaps, A, B, C, and D, as shown in Fig. 1. Cathode electrodes of the MWPCs are made of FR-4 fiberglass plates with two-sided 35 μm thick copper coating. Cathode plates of adjacent gaps are separated by honeycomb panels or rigid polyurethane foam which provide precise gap alignment over the whole chamber area. The general parameters of all MWPCs are the same: the anode planes are centered inside 5 mm gas gaps and are formed from 30 μm diameter gold-plated tungsten wires stretched with 2 mm steps. All MWPCs are filled with the 40% Ar + + 55% CO_2 + 5% CF_4 working gas mixture. The operation gas gain ranges between $4.6 \cdot 10^4$ and $8.8 \cdot 10^4$, depending on the high voltage settings. Each MWPC gap has an independent high-voltage channel. The gas mixture is supplied into the gaps sequentially, as is shown in Fig. 1.
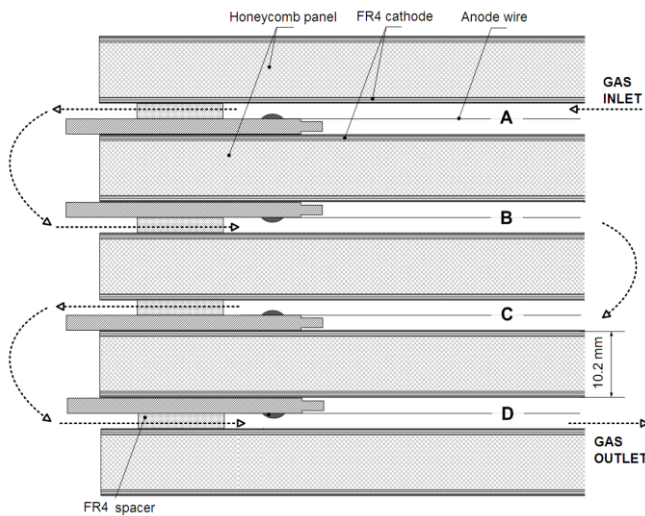
Fig. 1. Cross section of the LHCb muon chamber

Since the beginning of the LHCb operation, up to 17% of the muon detector modules experienced operation problems caused by the ME. In average, about 100 MWPC gaps suffer every year from high Malter currents and the concomitant high voltage trips. Nevertheless, all those problematic modules were successfully recovered *in situ*, under the nominal LHC beam conditions by means of a long-term high voltage training with the working gas mixture.

The gaps affected by the ME were trained during data taking. To increase concentration of fluorine radicals, *i. e.* to make the training more efficient, a sufficiently high Malter current should be supported in the damaged zone.

The training session starts with a slightly increased high voltage which provokes a rapid appearance of the Malter current from the problematic region. Usually the initial voltage values do not exceed 20–30 V above the nominal working point. During the training, the high voltage is varied to support the current at the level of ~ 40 μA.

A MWPC is considered to be restored when the current at the operating voltage reaches the nominal value corresponding to the LHC beam conditions (100–200 nA), and, when the beam drops, the current in the chamber also drops to zero. The duration of the training procedure for restoring a single ME spot in the proportional chamber may vary from one week to several months. A typical MWPC recovery under the high voltage training is demonstrated in Fig. 2. The bottom plot shows a history of changes of the high voltage which supported a reasonable level of the Malter current during the training procedure (*top plot*). As a result of the training, the self-sustained current dropped down to zero, and the nominal beam current ($I_{nom} \approx 140$ nA) was obtained at the working voltage ($V_{nom} = 2\,600$ V). The total duration of the presented recovery procedure is rather short – five days. On a statistical basis, the results of the training procedure are very positive – more than 90% of the MWPC suffered from the ME were restored to their normal behaviour.
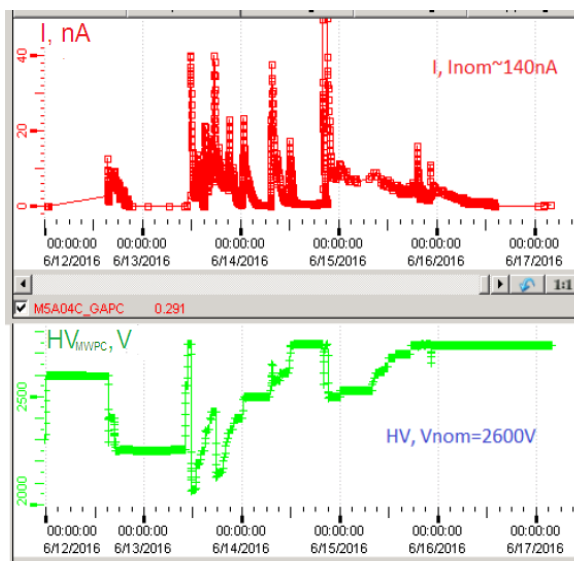
Fig. 2. Typical recovery procedure from the ME at the beam

With all the success of this method, the long duration of the training procedure greatly complicates the possibilities of its application. That is why it was proposed to use an oxygen admixture during the training procedure in order to accelerate the chamber recovery.

4. Gas composition for accelerated recovery from the Malter effect

Various studies of silicon dry etching processes showed that the etching rate in the CF_4–O_2 mixture is significantly higher than that in the pure CF_4 plasma [7–10, 12]. Oxygen radicals promote formation of $^\bullet COF_x$, which quickly dissociates in collisions with surrounding electrons and atoms (see Eqs. (7–10)), and indirectly increase the number of fluorine radicals in the gas discharge plasma:

$$O^\bullet + {}^\bullet CF_3 \rightarrow {}^\bullet COF_2 + F^\bullet; \tag{7}$$

$$O^\bullet + {}^\bullet CF_2 \rightarrow {}^\bullet COF + F^\bullet; \tag{8}$$

$$e^- + COF_2 \rightarrow {}^\bullet COF + F^\bullet + e^-; \tag{9}$$

$$O^\bullet + {}^\bullet COF \rightarrow CO_2 + F^\bullet. \tag{10}$$

The highest silicon etch rate is obtained in the CF_4–O_2 mixtures with the oxygen content from 10 to 30% [7–10]. Moreover, oxygen plays a significant role in polymer film dry etching with CF_4–O_2 mixtures [11] and may even be sufficient in some cases for dielectric deposition cleaning in the pure O_2 plasma [13].

Kinetics of chemical reactions in MWPC gas discharges may significantly differ from reactions rates in industrial reactors due to different plasma nature, gas pressure and electric field configuration. In MWPCs, the electric field varies from $E \approx 5$–6 kV · cm^{-1} on the cathode surface up to $E \approx 150$–200 kV · cm^{-1} on the anode wire. In industrial etching set-ups, the electric field is uniform and amounts to 10–50 kV · cm^{-1}, and a silicon wafer (to be etched) is placed in the plasma rich of active radicals. In proportional chambers, radicals are produced close to the anodes, which are separated from the cathodes with several millimeters of a low field region. Moreover, gas-discharge detectors usually operate with gas mixtures at the atmospheric pressure, which is several orders of magnitude higher than the pressure in industrial plasma reactors.

Nevertheless, even though the molecules and radicals in MWPCs have significantly smaller mean free path between electron collisions (~ 1 μm), the average electron energy (5–10 eV) is quite similar for both proportional chambers and reactors [14]. This makes possible to use dry etching chemical models in qualitative predictions for chemical processes in MWPCs.

Reactions of oxygen impact dissociation and excitation significant at this electron energy range are given below. The oxygen radical production in dissociative electron attachment by O_2 molecules (Eq. (11)) happens already at the electron energies ~ 5 eV, while, for example, the CO_2 electron impact dissociation starts only at ~ 13 eV [15]. Both, the atomic oxygen, $O^{..}$, and the excited molecular oxygen $^*O_2$, formed in collisions with electrons (Eq. 12), are chemically aggressive:

$$e^- + O_2 \rightarrow O^- + O^{..}, \tag{11}$$
$$e^- + O_2 \rightarrow {}^*O_2 + e^-. \tag{12}$$

The atomic oxygen $O^{..}$ interacts with O_2 molecules forming ozone:

$$O^{..} + O_2 \rightarrow O_3^*. \tag{13}$$

The excited ozone molecule, O_3^*, loses the excess energy through interaction with the plasma. The ground state ozone, O_3, can participate in processes of plasma chemistry etching on the cathode surface or recombines with free oxygen radicals:

$$O_3 + O^{..} \rightarrow 2O_2. \tag{14}$$

In contrast to the plasma reactor case, the O_2 content in the MWPC working gas mixture should be strongly limited due to the high oxygen electron attachment coefficient. Oxygen reduces the electron density in the discharge plasma, which results in reduction of the charge amplification. Therefore, to keep the gas gain at the level sufficient for the recovery process, the oxygen content should be optimized.

To find the optimal amount of oxygen additive in the working gas mixture, simulation studies for muon detector MWPCs were performed using the GARFIELD software package. The results of the simulation are shown in Fig. 3. The electron attachment coefficient as a function of the electric field strength is shown in the top plot. The bottom plot demonstrates the gas gain dependence on the oxygen content in the 40% Ar + 55% CO_2 + + 5% CF_4 gas mixture. Figure 3 (*top*) shows that for 1–4% of the O_2 content the electron attachment coefficient increases substantially only in the drift region, especially near the cathode surface, where the electric field strength is about $6\,000\,\text{kV} \cdot \text{cm}^{-1}$. When the oxygen content exceeds 10%, a noticeable electron attachment occurs throughout the whole drift path and in the avalanche region. As a result, the MWPC gas gain at the operation voltage drops by more than 60%, as can be seen in Fig. 3 (*bottom*). Under such conditions, the charging of a dielectric deposit film on the cathode surface will be slowed

Fig. 3. Electron attachment coefficient as a function of the electric field strength (*top*); the gas gain as a function of the oxygen content (*bottom*)

down, which reduces the Malter current. A too small current cannot support an effective etching process. According to the GARFIELD predictions, to compensate for such a gain reduction, the high voltage should

be increased up to 3 000 V, that is above the safe operation range. Therefore, the oxygen content in the gas mixture used for the recovery procedure is a compromise between the acceleration of training and the voltage increase needed to compensate for the gas gain drop caused by the presence of oxygen.

5. Accelerated recovery of muon multi-wire proportional chambers with the gas mixture containing oxygen

To test the ME suppressing procedure with an oxygen-containing gas mixture, four modules of the muon detector were chosen. These modules were removed from the experimental set-up because of high ME currents impeding their proper operation and due to multiple fails of the standard recovery procedure with the nominal working gas mixture.

Localization of the ME zones on cathodes of the damaged MWPC gaps were performed with a collimated ^{90}Sr ($E_\beta = 2.28$ MeV) β source. The Malter currents ignited by the source were hundred times larger than the ionization current. As a result of thorough scans performed for each of the four MWPC of every module, seven ME zones were identified.

The recovery training with an oxygenated gas mixture was performed for each of those zones. The ^{90}Sr β source irradiated the recovering area to ignite and to support the Malter currents. The training was identical to the one described in Section 3. Supporting a few tens microampere current during the training resulted in the accelerated recovery of all ME zones. The recovery procedure is based on the plasma-chemical etching of silicon and organic compounds by fluoride, oxygen active radicals and ozone produced in the gas discharge. Volatile compounds formed during the etching were removed in the process of gas flushing [4].

Figure 4 shows the currents caused by the ME as a function of the training time for the nominal 40% Ar + 55% CO_2 + 5% CF_4 gas mixture (*red rhombuses*) and for the nominal gas mixture enriched with two percent oxygen (*blue circles*). An initial Malter current of 25 µA was ignited by the ^{90}Sr β source at the voltage of 2 600–2 700 V and was maintained by increasing the voltage in 50 V steps. The ME current decreases as the dielectric film is being removed from the cathode surface. The total time required to recover the ME zone in the case of the oxygen-containing mixture was around 4 h. However, with the nominal working mixture the Malter current stays constant even after more than 6 h [4].
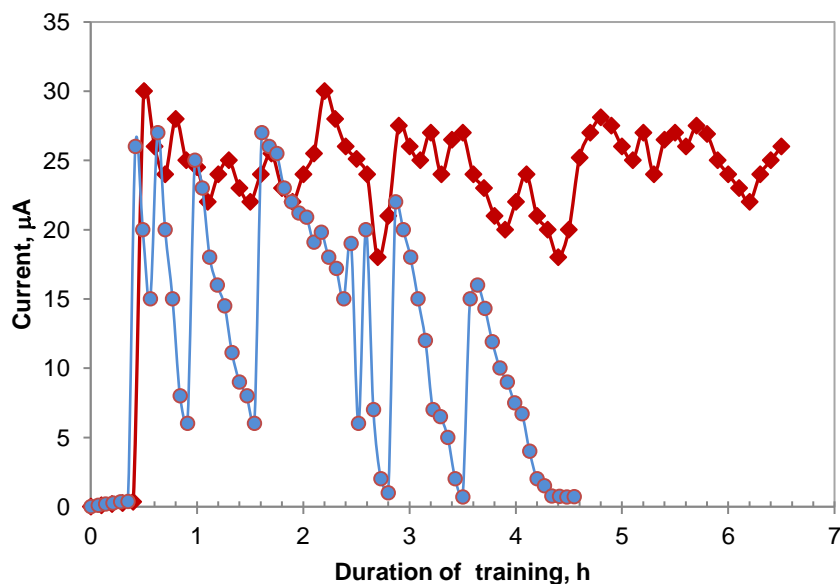
Fig. 4. Current in the MWPC during the ME suppression training

6. Conclusion

- Adding of oxygen to the Ar–CO_2–CF_4 gas mixture allow us to speed up the ME suppression training hundreds of times.
- The given technique allows several times to increase the durability of the MWPC operation in the field of intensive irradiation.
- The non-invasive character of the recovery technique makes it actual for many experiments where the detectors operate with the gas mixtures containing CO_2 and CF_4.

References

1. M. Capeans, Nucl. Instrum. Meth. Phys. Res. A **515**, 73 (2003).
2. S. Belostotski *et al.*, Nucl. Instrum. Meth. Phys. Res. A **591**, 353 (2008).
3. L. Malter, Phys. Rev. **50**, 48 (1936).
4. G.E. Gavrilov *et al.*, Phys. Elem. Particles Atom. Nucl. **49**, No. 1, 33 (2018).
5. J. Va'vra, Nucl. Instrum. Meth. Phys. Res. A **515**, 1 (2003).
6. G.E. Gavrilov, V.M. Vakhtel *et al.*, Phys. Atom. Nucl. **80**, No. 9, 1 (2017).
7. J.W. Coburn, *Plasma Etching and Reactive Ion Etching*, Am. Vacuum Soc., New York, 1982.
8. K.R. Ryan, I.C. Plumb, Plasma Chem. Plasma Process. **6**, Iss. 3, 205 (1986).
9. Yu.N. Grigoryev, A.G. Gorobchuk, Comput. Technol. **8**, No. 2, 53 (2003).
10. F.I. Grigoryev, *Plasma-Chemical and Ion-Chemical Etching in Microelectronics Technology, Textbook,* Mosc. Gos. Univ., Elektron. Mat., Moscow, 2003 [in Russian].
11. M.D. Koretsky, J.A. Reimer, J. Appl. Phys., **72**, No. 11, 5081 (1992).
12. C.J. Mogab, A.C. Adams, D.L. Flamm, J. Appl. Phys. **49**, 3796 (1978).
13. Boing Aerospace Research & Engineering Div., Active Cleaning Technique for Removing Contamination from Optical Surface in Space, Final Report D180-17610-1, Contract NAS8-26385, Siettle, Washington, 98124, Aug. 1973.
14. J. Va'vra, Nucl. Instrum. Meth. Phys. Res. A **252**, 547 (1986).
15. J.W. McConkey, C.P. Malone, P.V. Johnson *et al*., Phys. Rep. **466**, 1 (2008).

CONTENTS

PNPI PARTICIPATION IN THE LHC DETECTORS UPGRADE

NUCLEAR AND ATOMIC PHYSICS

NEW PROJECTS

METHODICAL AND APPLIED RESEARCH

High Energy Physics Division
MAIN SCIENTIFIC ACTIVITIES
2013–2018